

AD-A116 453

OHIO STATE UNIV COLUMBUS ELECTROSCIENCE LAB
GEODESIC PATHS OF AN ELLIPSOID-MOUNTED ANTENNA. (U)
MAR 82 J S KIM, N WANG, C D CHUANG
ESL-714215-1

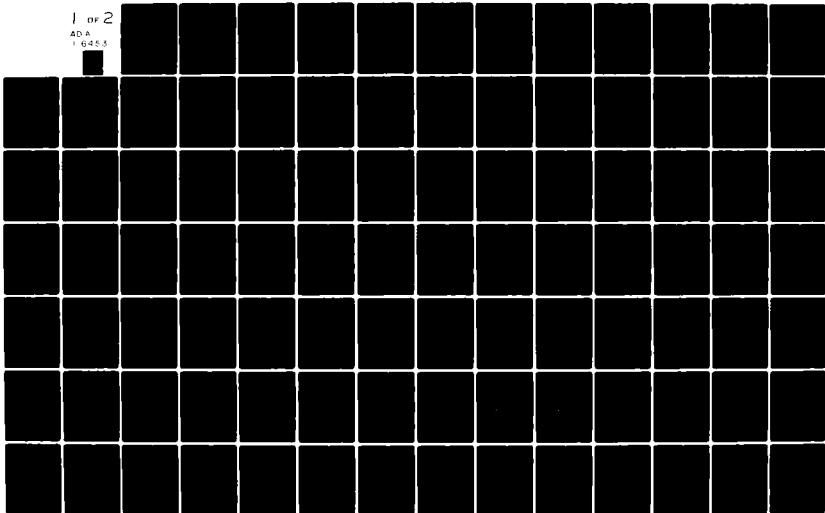
F/6 9/1

N00019-81-C-0424

NL

UNCLASSIFIED

1 of 2
AD A
1 6453



AD A116453



The Ohio State University

GEODESIC PATHS OF AN
ELLIPSOID-MOUNTED ANTENNA

Jeung G. Kim
Nan Wang
C.D. Chuang

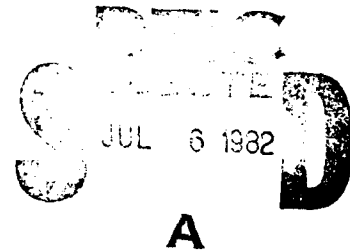
The Ohio State University
ElectroScience Laboratory

Department of Electrical Engineering
Columbus, Ohio 43212

Technical Report 714215-1

Contract N00019-81-C-0424

March 1982



APPROVED FOR PUBLIC RELEASE
DISTRIBUTION UNLIMITED

Department of the Navy
Naval Air Systems Command
Washington, D.C. 20361

82 00 00 178

NOTICES

When Government drawings, specifications, or other data are used for any purpose other than in connection with a definitely related Government procurement operation, the United States Government thereby incurs no responsibility nor any obligation whatsoever, and the fact that the Government may have formulated, furnished, or in any way supplied the said drawings, specifications, or other data, is not to be regarded by implication or otherwise as in any manner licensing the holder or any other person or corporation, or conveying any rights or permission to manufacture, use, or sell any patented invention that may in any way be related thereto.

REPORT DOCUMENTATION PAGE 1. REPORT NO. AD-A116 453		3. Recipient's Accession No.	
4. Title and Subtitle GEODESIC PATHS OF AN ELLIPSOID-MOUNTED ANTENNA		5. Report Date March 1982	
7. Author(s) J.G. Kim, N. Wang, C.D. Chuang		8. Performing Organization Rept. No. ESL 714215-1	
9. Performing Organization Name and Address The Ohio State University ElectroScience Laboratory Department of Electrical Engineering Columbus, Ohio 43212		10. Project/Task/Work Unit No. 11. Contract(C) or Grant(G) No. (C) N00019-81-C-0424 (G)	
12. Sponsoring Organization Name and Address Department of the Navy Naval Air Systems Command Washington, D.C. 20361		13. Type of Report & Period Covered Technical	
14.			
15. Supplementary Notes			
16. Abstract (Limit: 200 words) <p>In applying the high frequency ray technique (GTD) to the radiation problems of an Ellipsoid-mounted antenna, it is essential to determine the geodesic paths on the surface. An efficient, approximate solution for the geodesic paths on the ellipsoid surface, which in turn can be used to model an aircraft or missile fuselage is studied here. Another elaborate method for the geodesic paths employing the calculus of variations is also presented to show the validity of the approximation solution. Typical ellipsoid geometries were chosen and tested for various antenna locations on those surfaces. Good agreement between both methods within the significant energy region confirms that the geodesic paths are efficiently solved via this numerical approach.</p>			
17. Document Analysis a. Descriptors			
b. Identifiers/Open-Ended Terms Electromagnetic Radiation, Geometrical Theory of Diffraction, Geodesic Path, Geodesic Tangent, Elliptic Cone Perturbation, Elliptic Cylinder Perturbation, Exact Solution, Fock parameter, Principal direction			
c. COSATI Field/Group			
18. Availability Statement APPROVED FOR PUBLIC RELEASE DISTRIBUTION UNLIMITED		19. Security Class (This Report) Unclassified	21. No. of Pages 99
		20. Security Class (This Page) Unclassified	22. Price

TABLE OF CONTENTS

	Page
LIST OF TABLES	iv
LIST OF FIGURES	v
CHAPTER I: INTRODUCTION	1
CHAPTER II: THEORETICAL BACKGROUND	6
A. Introduction	6
B. Shadow Region	7
C. Lit Region	14
D. Pattern Factors	18
E. Ellipsoid Surface Parameters	19
CHAPTER III: NUMERICAL TECHNIQUE AND PERTURBATION METHOD	27
A. Introduction	27
B. Surface Geodesics	28
C. Elliptic Cylinder Perturbation	34
D. Elliptic Cone Perturbation	38
CHAPTER IV: EXACT GEODESIC PATHS OF AN ELLIPSOID	46
CHAPTER V: RESULTS	53
CHAPTER VI: SUMMARY AND CONCLUSIONS	70
REFERENCES	88

iii

A

DTIC
COPY
INSPECTED
2

LIST OF TABLES

Table		Page
I	For Shadow Region	11
II	For Lit Region	18

LIST OF FIGURES

Figure		Page
1	Ray path in the shadow region.	2
2	The region of significant energy flow from an antenna mounted on an ellipsoid.	4
3(a)	Elliptic cone simulation.	5
3(b)	Elliptic cone perturbation model.	5
4	Surface diffracted ray tube and ray coordinates for the shadow region.	8
4(a)	Perspective view of a surface diffracted ray tube (enlarged view).	8
4(b)	Top view of diffracted ray tube indicating the divergence of the rays and the unit binormal vectors at Q' and Q .	8
4(c)	Side view of surface diffracted ray tube and the unit normal and tangent vectors at Q' and Q .	8
5	Ray tube and ray coordinates.	15
6	Geometry of an ellipsoid.	20
7	Geodesic path on an ellipsoid.	22
8	Geodesic path on a developed elliptic cylinder.	29
8(a)	True elliptic cylinder.	29
8(b)	Unfolded planar surface.	29
9	Geodesic path on a developed elliptic cone.	31

Figure		Page
9(a)	True elliptic cone.	31
9(b)	Unfolded planar surface.	31
10(a)	Geodesic path on an ellipsoid.	32
10(b)	Elliptic profile.	33
11	Geodesic path on the perturbed elliptic cone.	39
12	Geodesic path on the unfolded elliptic cone.	40
13(a)	Elliptic profile.	42
13(b)	Elliptic cone.	43
13(c)	Unfolded planar surface of the elliptic cone.	43
14	Projection of ϕ - and ψ - curves onto the xz plane on an ellipsoid.	54
15(a)	Illustration of the geodesic path defined by the surface parameters (θ_Q, ϕ_Q) for the source mounted on an ellipsoid.	55
15(b)	Illustration of the geodesic tangent defined by the radial vector direction (θ_t, ϕ_t) for the source mounted on an ellipsoid.	55
16(a)	Geodesic paths defined by the surface parameters (θ_Q, ϕ_Q) for a source mounted at $\theta_S=90^\circ$ on a $2\lambda \times 3\lambda \times 4\lambda$ ellipsoid.	57
16(b)	Geodesic paths defined by the surface parameters (θ_Q, ϕ_Q) for a source mounted at $\theta_S=90^\circ$ on a $2\lambda \times 3\lambda \times 20\lambda$ ellipsoid.	58

Figure		Page
16(c)	Geodesic paths defined by the surface parameters (θ_Q, ϕ_Q) for a source mounted at $\theta_S=90^\circ$ on a $2\lambda \times 4\lambda \times 20\lambda$ ellipsoid.	59
16(d)	Geodesic paths defined by the surface parameters (θ_Q, ϕ_Q) for a source mounted at $\theta_S=90^\circ$ on a $4\lambda \times 6\lambda \times 40\lambda$ ellipsoid.	60
17(a)	Geodesic tangents defined by the radial vector direction (θ_t, ϕ_t) for a source mounted at $\theta_S=90^\circ$ on a $2\lambda \times 3\lambda \times 4\lambda$ ellipsoid.	61
17(b)	Geodesic tangents defined by the radial vector direction (θ_t, ϕ_t) for a source mounted at $\theta_S=90^\circ$ on a $2\lambda \times 3\lambda \times 20\lambda$ ellipsoid.	62
17(c)	Geodesic tangents defined by the radial vector direction (θ_t, ϕ_t) for a source mounted at $\theta_S=90^\circ$ on a $2\lambda \times 4\lambda \times 20\lambda$ ellipsoid.	63
17(d)	Geodesic tangents defined by the radial vector direction (θ_t, ϕ_t) for a source mounted at $\theta_S=90^\circ$ on a $4\lambda \times 6\lambda \times 40\lambda$ ellipsoid.	64
18(a)	Geodesic paths defined by the surface parameters (θ_Q, ϕ_Q) for a source mounted at $\theta_S=30^\circ$ on a $2\lambda \times 3\lambda \times 4\lambda$ ellipsoid.	65
18(b)	Geodesic paths defined by the surface parameters (θ_Q, ϕ_Q) for a source mounted at $\theta_S=30^\circ$ on a $2\lambda \times 3\lambda \times 8\lambda$ ellipsoid.	66

Figure		Page
18(c)	Geodesic paths defined by the surface parameters (θ_Q, ϕ_Q) for a source mounted at $\theta_S=30^\circ$ on a 4 λ x6 λ x40 λ ellipsoid.	67
18(d)	Geodesic paths defined by the surface parameters (θ_Q, ϕ_Q) for a source mounted at $\theta_S=85^\circ$ on a 4 λ x6 λ x40 λ ellipsoid.	68
19(a)	Geodesic tangents defined by the radial vector direction (θ_t, ϕ_t) for a source mounted at $\theta_S=30^\circ$ on a 2 λ x3 λ x4 λ ellipsoid.	71
19(b)	Geodesic tangents defined by the radial vector direction (θ_t, ϕ_t) for a source mounted at $\theta_S=45^\circ$ on a 2 λ x3 λ x4 λ ellipsoid.	72
19(c)	Geodesic tangents defined by the radial vector direction (θ_t, ϕ_t) for a source mounted at $\theta_S=60^\circ$ on a 2 λ x3 λ x4 λ ellipsoid.	73
19(d)	Geodesic tangents defined by the radial vector direction (θ_t, ϕ_t) for a source mounted at $\theta_S=80^\circ$ on a 2 λ x3 λ x4 λ ellipsoid.	74
19(e)	Geodesic tangents defined by the radial vector direction (θ_t, ϕ_t) for a source mounted at $\theta_S=30^\circ$ on a 2 λ x3 λ x8 λ ellipsoid.	75
19(f)	Geodesic tangents defined by the radial vector direction (θ_t, ϕ_t) for a source mounted at $\theta_S=45^\circ$ on a 2 λ x3 λ x8 λ ellipsoid.	76

Figure		Page
19(g)	Geodesic tangents defined by the radial vector direction (θ_t, ϕ_t) for a source mounted at $\theta_s=60^\circ$ on a $2\lambda \times 3\lambda \times 8\lambda$ ellipsoid.	77
19(h)	Geodesic tangents defined by the radial vector direction (θ_t, ϕ_t) for a source mounted at $\theta_s=80^\circ$ on a $2\lambda \times 3\lambda \times 8\lambda$ ellipsoid.	78
19(i)	Geodesic tangents defined by the radial vector direction (θ_t, ϕ_t) for a source mounted at $\theta_s=30^\circ$ on a $2\lambda \times 3\lambda \times 10\lambda$ ellipsoid.	79
19(j)	Geodesic tangents defined by the radial vector direction (θ_t, ϕ_t) for a source mounted at $\theta_s=30^\circ$ on a $2\lambda \times 3\lambda \times 11\lambda$ ellipsoid.	80
19(k)	Geodesic tangents defined by the radial vector direction (θ_t, ϕ_t) for a source mounted at $\theta_s=30^\circ$ on a $2\lambda \times 3\lambda \times 12\lambda$ ellipsoid.	81
19(l)	Geodesic tangents defined by the radial vector direction (θ_t, ϕ_t) for a source mounted at $\theta_s=30^\circ$ on a $2\lambda \times 3\lambda \times 20\lambda$ ellipsoid.	82
19(m)	Geodesic tangents defined by the radial vector direction (θ_t, ϕ_t) for a source mounted at $\theta_s=45^\circ$ on a $2\lambda \times 3\lambda \times 20\lambda$ ellipsoid.	83
19(n)	Geodesic tangents defined by the radial vector direction (θ_t, ϕ_t) for a source mounted at $\theta_s=60^\circ$ on a $2\lambda \times 3\lambda \times 20\lambda$ ellipsoid.	84

Figure		Page
19(o)	Geodesic tangents defined by the radial vector direction (θ_t, ϕ_t) for a source mounted at $\theta_s=80^\circ$ on a $2\lambda \times 3\lambda \times 20\lambda$ ellipsoid.	85
19(p)	Geodesic tangents defined by the radial vector direction (θ_t, ϕ_t) for a source mounted at $\theta_s=30^\circ$ on a $4\lambda \times 6\lambda \times 40\lambda$ ellipsoid.	86

CHAPTER I

INTRODUCTION

In applying the Geometrical Theory of Diffraction (GTD) to antenna radiation and coupling problems involving curved surfaces. A major task is to determine the geodesic paths on the curved surface. For airborne antennas mounted on the fuselage of an aircraft, the fuselage is generally modeled as a cylinder or a prolate spheroid [1,2] in the GTD analysis. However to better approximate general fuselage shapes, an ellipsoidal model of the fuselage is needed. Among the solutions for obtaining the geodesic paths of the three models, i.e., the cylindrical, the prolate spheroidal and the ellipsoidal models, the ellipsoid case is the most involved and complex one. This is to be expected because the equation describing an ellipsoid can degenerate into that of a cylinder or a prolate spheroid by using appropriate parameters.

According to the generalized Fermat's principle, a ray emanating from a source, which is located on the surface, follows a geodesic path on the surface and continually sheds energy into the shadow region. Such a creeping wave mechanism is illustrated in Figure 1, from which it can be seen that a ray traverses from the source point Q' to the diffraction point Q , and then propagates along the geodesic tangent at Q toward the observation point P_s .

As the energy flows around the surface, it is continuously diffracted along the geodesic tangent toward the field point such that

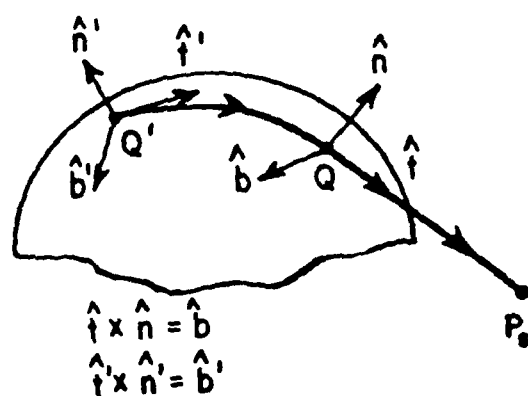


Figure 1. Ray path in the shadow region.

the significant effect of the surface is associated with a region around the source. In fact, for an ellipsoid, the significant portion of the surface, which is associated with the dominant energy, may look as shown in Figure 2.

Note that this region can be specified by following the various geodesic paths until the radiation level along a given path becomes insignificant, i.e., more than 40db below the source magnitude. With this in mind, it is clear that one could represent the ellipsoid by a structure which simulates the elliptic cross section completely; however, the profile could be approximated by a simpler shape since the significant energy region does not cover a large portion of the profile shape. An elliptic cone model is employed here to simulate the ellipsoid which in turn can be used to model a fuselage. This perturbation model is illustrated in Figure 3 for a source located near one end of the ellipsoid. Note that if the source is placed at the center of the ellipsoid, the elliptic cone actually becomes a right elliptic cylinder.

Since the elliptic cone is a developed surface, one can unfold the elliptic cone such that a planar structure results. The geodesics associated with the elliptic cone are, then, straight lines on this planar structure. In order to allow for a geodesic solution between the simplicity of the elliptic cone and the rigor of the ellipsoid, one can perturb the elliptic cone by bending it along its generator as illustrated in Figure 3(b). In that a perturbation technique is employed, the geodesic paths for the elliptic cone are simply modified such

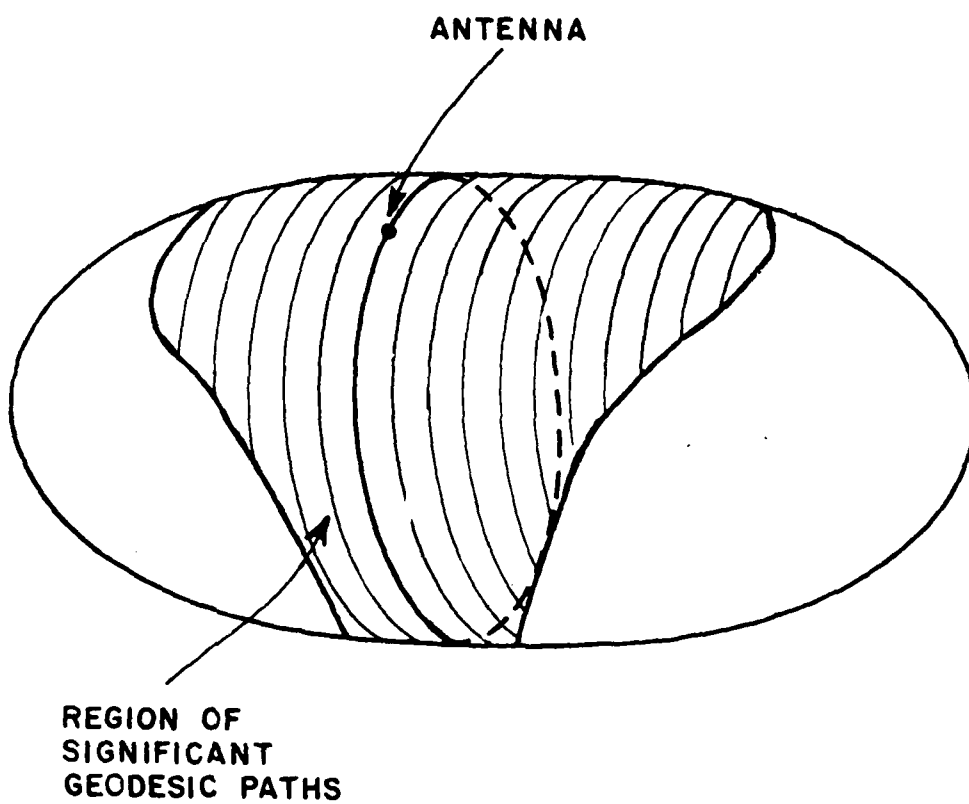


Figure 2. The region of significant energy flow from an antenna mounted on an ellipsoid.

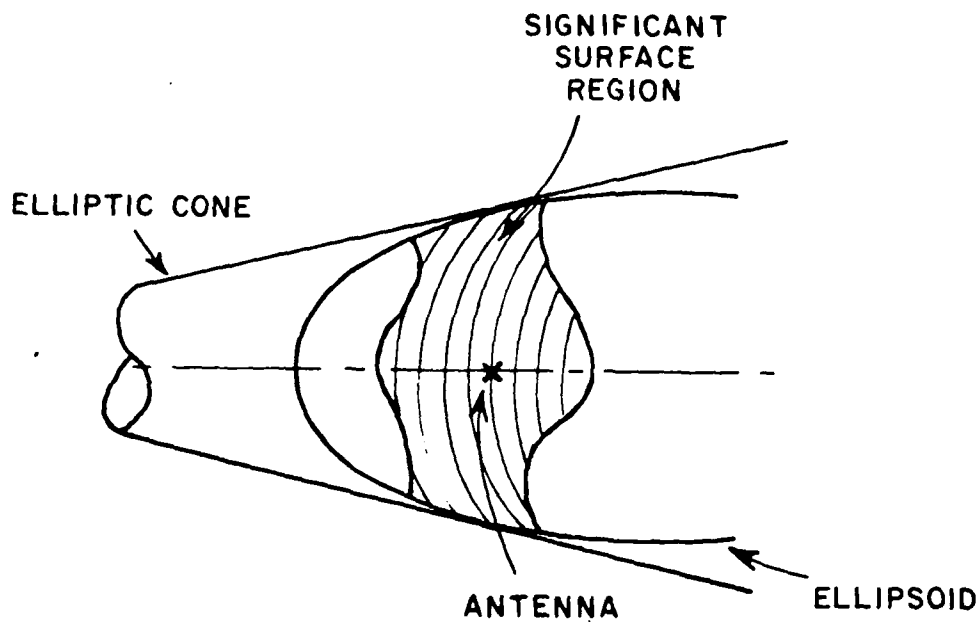


Figure 3(a). Elliptic Cone simulation.

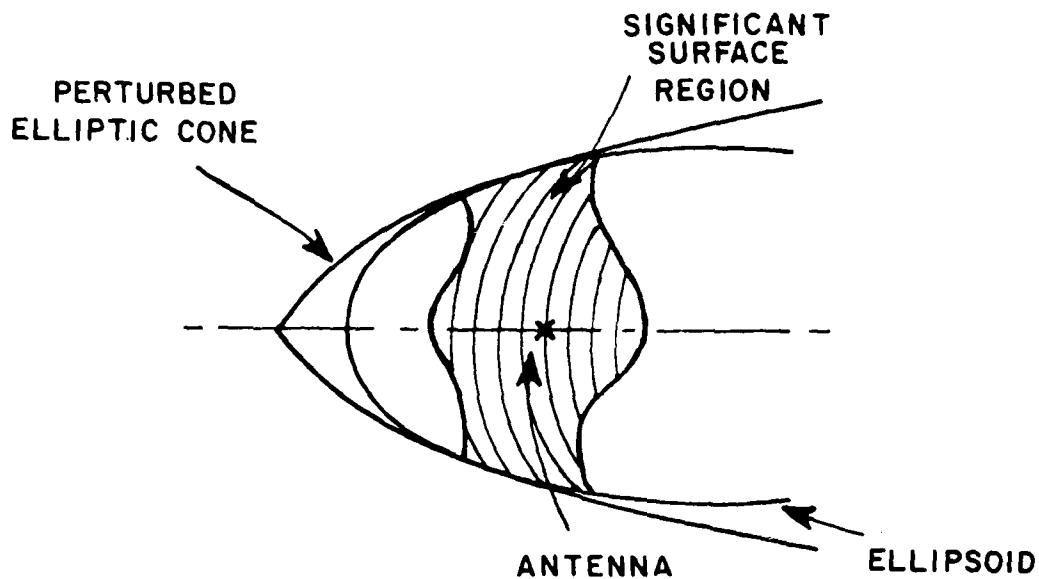


Figure 3(b). Elliptic Cone perturbation model.

that the solution for the ellipsoid is basically straight-forward and is the basis for this report. It is obvious that one cannot use this perturbation technique if significant energy propagates far away from the source. However, as mentioned previously, the energy which propagates great distances along the ellipsoid surface becomes insignificant in magnitude such that one need not solve for the true geodesic paths outside the significant region shown in Figure 3(b). The simplicity of these perturbed geodesic paths allows one to very efficiently determine the significant ray paths on the ellipsoid.

CHAPTER II

THEORETICAL BACKGROUND

A. Introduction

The radiated field of an ellipsoid-mounted antenna is analyzed using the Geometrical Theory of Diffraction (GTD). The surface is assumed to be perfectly conducting, and the surrounding medium is free space. An $\exp(j\omega t)$ time dependence is understood and suppressed in the following formulations.

Consider an infinitesimal, magnetic current moment $d\vec{P}_m(Q')$ or an electric current moment $d\vec{P}_e(Q')$ located on a perfectly conducting convex surface as shown in Figure 1; the sources

$$d\vec{P}_m(Q') = \vec{E}(Q') \times \hat{n}' da'$$

$$\text{and } d\vec{P}_e(Q') = I(\ell') d\ell' \hat{n}'$$

pertain to the aperture and monopole type excitations with

$\vec{E}(Q')$ = electric field at Q' ,

\hat{n}' = outward unit surface normal at Q' ,

da' = area element at Q' ,

$I(\ell')$ = electric current distribution on the monopole, and

ℓ' = distance parameter along the monopole.

According to geometrical optics, the space surrounding the source is divided into an illuminated and shadow region by a plane tangent to the surface at Q' . This plane is referred to as a shadow boundary. Since the field in the deep lit region is essentially that obtained from geometrical optics, and the field in the deep shadow region is relatively weak, the solution for the transition region adjacent to the shadow boundary is of more interest and discussed below.

B. Shadow Region

The creeping wave mechanism in the shadow region is illustrated in Figure 4. From the generalized Fermat's principle, a ray emanating from the source $d\vec{P}_m(Q')$ at Q' traverses a geodesic path $Q'Q$ on the surface, and propagates along the geodesic tangent at Q toward the field point P_s . The field $d\vec{E}_m$ at P_s can be expressed in terms of the field at a reference point P_0 by [3]

$$d\vec{E}_m(P_s) \sim d\vec{E}_m(P_0) \sqrt{\frac{\frac{d}{\rho_1} \frac{d}{\rho_2}}{\left(\frac{d}{\rho_1+s_0}\right) \left(\frac{d}{\rho_2+s_0}\right)}} e^{-jks_0} + O[m^{-2}, m^{-3}] \quad (1)$$

where

ρ_1^d and ρ_2^d are the principal radii of curvatures of the wavefront at P_0 ;

and $O[m^{-2}, m^{-3}, \dots]$ are the higher order terms.

From Figure 4, it is seen that if the reference point P_0 is moved to the curved surface diffraction point Q , then $\rho_1^d \rightarrow 0$, $\rho_2^d \rightarrow \rho_c$, and $s_0 \rightarrow s$. Since $d\bar{E}_e(P_s)$ is independent of the reference point P_0 , it follows that

$$\lim_{\substack{P_0 \rightarrow Q \\ \rho_1^d \rightarrow 0}} \sqrt{\rho_1^d} d\bar{E}_e(P_0) = \bar{L}_m(Q', Q) ; \quad (2)$$

then,

$$d\bar{E}_e(P_s) \sim \bar{L}_m(Q', Q) \sqrt{\frac{\rho_c}{s(\rho_c + s)}} e^{-jks} . \quad (3)$$

Furthermore, $\bar{L}_m(Q', Q)$ can be related to the source strength $d\bar{P}_m$ at Q' by

$$\bar{L}_m(Q', Q) = d\bar{P}_m(Q') \cdot \bar{T}_m(Q', Q) \quad (4)$$

where $\bar{T}_m(Q', Q)$ is given by [3]

$$\bar{T}_m(Q', Q) = \frac{-jk}{4\pi} [\hat{b}' \hat{n} T_1(Q') H + \hat{t}' \hat{b} T_2(Q') S + \hat{b}' \hat{b} T_3(Q') S + \hat{t}' \hat{n} T_4(Q') H]$$

$$e^{-jkt} \sqrt{\frac{d\psi_0}{d_n(Q)}} \left[\frac{\rho_g(Q)}{\rho_g(Q')} \right]^{1/6} \quad (5)$$

$$\bar{T}_e(Q', Q) = \frac{-jkZ_0}{4\pi} [\hat{n}' \hat{n} T_5(Q') H + \hat{n}' \hat{b} T_6(Q') S] e^{-jkt}$$

$$\sqrt{\frac{d\psi_0}{d_n(Q)}} \left[\frac{\rho_g(Q)}{\rho_g(Q')} \right]^{1/6} \quad (6)$$

Here $(\hat{t}', \hat{n}', \hat{b}')$ and $(\hat{t}, \hat{n}, \hat{b})$ are the tangent, normal and binormal unit vectors to the surface at the source point (Q') and diffraction point (Q) , respectively. As seen from Figure 4, $\hat{t} \times \hat{n} = \hat{b}$ and $\hat{t}' \times \hat{n}' = \hat{b}'$. The quantities $T_1(Q')$, ..., $T_6(Q')$ are the torsion factors at Q' and are given in Table 1. Also,

$$H = g(\xi) \quad (7)$$

$$S = \frac{-j}{m(Q')} \tilde{g}(\xi) \quad (8)$$

with

$$g(\xi) = \frac{1}{\sqrt{\pi}} \int_{-\infty}^{\infty} \exp(-j2\pi/3) \frac{\exp(-j\tau\xi)}{w_2(\tau)} d\tau \quad \text{and} \quad (9)$$

TABLE 1
(FOR SHADOW REGION)

TYPE OF CONVEX SURFACE	SLOT OR $d\vec{p}_m$ CASE				MONOPOLE OR $d\vec{p}_0$ CASE		SURFACE RAY TORSION $T(Q')$	SURFACE RADIUS OF CURVATURE IN $\hat{\tau}$ DIRECTION $\rho_0(Q')$	SURFACE DIFFRACTED RAY CAUSTIC DISTANCE ρ_c
	$T_1(Q')$	$T_2(Q')$	$T_3(Q')$	$T_4(Q')$	$T_5(Q')$	$T_6(Q')$			
SPHERE	1	1	0	0	1	0	0	0	$a \tan(\frac{1}{2})$
CIRCULAR CYLINDER	1	1	$\frac{\sin 2\alpha'}{2a} + \frac{a}{\sin^2 \alpha'}$	0	1	$\frac{\sin 2\alpha'}{2a} + \frac{a}{\sin^2 \alpha'}$	$\frac{\sin 2\alpha'}{2a}$	$\frac{a}{\sin^2 \alpha'}$	1
ARBITRARY CONVEX SURFACE	1	1	$T_1(Q')\rho_0(Q')$	0	1	$T_1(Q')\rho_0(Q')$	$\frac{\sin 2\alpha'}{2} \left(\frac{1}{R_2(Q')} - \frac{1}{R_1(Q')} \right)$ WITH $R_1(Q') \geq R_2(Q')$	$\left(\frac{\cot^2 \alpha'}{R_1(Q')} + \frac{\sin^2 \alpha'}{R_2(Q')} \right)^{-1}$	$\frac{2\sqrt{E} \cdot 0}{\partial \theta / \partial \tau}$

Note: (1) α' is defined by $\hat{\tau}_1' \cdot \hat{\tau}' = \cos \alpha'$ where $\hat{\tau}_1'$ is the principal direction unit vector associated with $R_1(Q')$.

(2) The quantities E and G denote two of the three coefficients E, F, G that appear in the "first fundamental form" of Differential Geometry [5].

$$\tilde{g}(\xi) = \frac{1}{\sqrt{\pi}} \int_{-\infty}^{\infty} \exp(-j2\pi/3) \frac{d\tau}{w_2'(\tau)} \exp(-j\tau\xi) \quad (10)$$

which are known as the acoustic hard and soft Fock functions. The Fock type Airy function is given by

$$w_2(\tau) = \frac{1}{\sqrt{\pi}} \int_{-\infty}^{\infty} \exp(j2\pi/3) dt \exp(\tau t - t^3/3) \quad (11)$$

and $w_2'(\tau)$ is the derivative of $w_2(\tau)$ with respect to τ . The Fock parameter ξ for the shadow region is given by [3]

$$\xi = \int_{Q'}^Q dt' \frac{m(t')}{\rho_g(t')} \quad (12)$$

with

$$m(t') = \left[\frac{k \rho_g(t')}{2} \right]^{1/3} \quad (13)$$

Here $\rho_g(t')$ is the surface radius of curvature along the ray path at t' .

The width of the surface ray tube at Q , $d\eta(Q)$, is given by

$$d\eta(Q) = \rho_c d\psi \quad (14)$$

Note the parameters Z_0 and t are defined as the free space wave impedance and geodesic arc length from Q' to Q , respectively.

Combining Equations (3)-(14), the \hat{n} and \hat{b} directed components of $d\vec{E}_m(P_s)$ are given by [3]

(a) $d\vec{P}_m(Q')$ case:

$$dE_m^n(P_s) = \frac{-jk}{4\pi} (d\vec{P}_m \cdot \hat{b}') He^{-jkt} \left[\frac{\rho_g(Q')}{\rho_g(Q)} \right]^{-1/6} \sqrt{\frac{d\psi_0}{d\psi}} \sqrt{\frac{1}{s(\rho_c+s)}} e^{-jks+0[m-2]} \quad (15)$$

$$dE_m^b(P_s) = \frac{-jk}{4\pi} [(d\vec{P}_m \cdot \hat{b})T_0 S + (d\vec{P}_m \cdot \hat{t}')S] e^{-jkt} \left[\frac{\rho_g(Q')}{\rho_g(Q)} \right]^{-1/6} \sqrt{\frac{d\psi_0}{d\psi}} \sqrt{\frac{1}{s(\rho_c+s)}} e^{-jks+0[m-2, m-3]} \quad (16)$$

(b) $dP_e(Q')$ case:

$$dE_e^n(P_s) = \frac{-jkZ_0}{4\pi} dP_e(Q') He^{-jkt} \left[\frac{\rho_g(Q')}{\rho_g(Q)} \right]^{-1/6} \sqrt{\frac{d\psi_0}{d\psi}} \sqrt{\frac{1}{s(\rho_c+s)}} e^{-jks+0[m-2]} \quad (17)$$

$$dE_e^b(P_s) = \frac{-jkZ_0}{4\pi} dP_e(Q') T_0 S e^{-jkt} \left[\frac{\rho_g(Q')}{\rho_g(Q)} \right]^{-1/6} \sqrt{\frac{d\psi_0}{d\psi}} \sqrt{\frac{1}{s(\rho_c+s)}} e^{-jks+0[m-2]} \quad (18)$$

where $T_0 = T(Q')\rho_g(Q')$ with $T(Q')$ being the surface torsion at the source location (refer to Table 1).

C. Lit Region

From geometrical optics, the source $d\bar{P}_m(Q')$ at Q' excites waves which propagate along straight line ray paths from the source to field point in the lit region. As shown in Figure 5, the field $d\bar{E}_m(P_L)$ at point P_L is expressed by

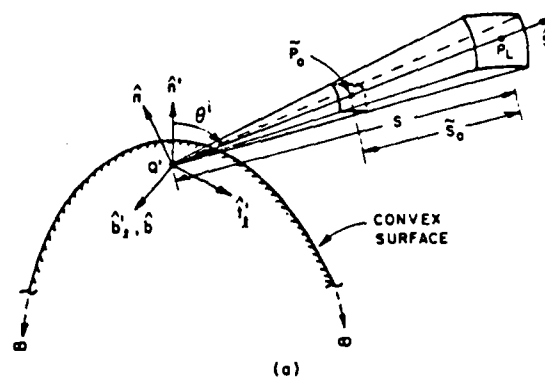
$$d\bar{E}_m(P_L) \sim d\bar{E}_m(P_0) \sqrt{\frac{\rho_1^i \rho_2^i}{(\rho_1^i + \tilde{s}_0)(\rho_2^i + \tilde{s}_0)}} e^{-jk\tilde{s}_0} + O[\ell^{-2}, \ell^{-3}] \quad (19)$$

Since Q' is the only caustic of the incident rays, the principal radii of curvature ρ_1^i and ρ_2^i associated with the incident wavefront at \tilde{P}_0 are identical, i.e., $\rho_1^i = \rho_2^i = \rho^i$. Furthermore, $d\bar{E}_m(P_L)$ is independent of the reference point \tilde{P}_0 . If \tilde{P}_0 is chosen to be at Q' , it follows that

$$\lim_{\substack{\tilde{P}_0 \rightarrow Q' \\ \rho^i \rightarrow 0 \\ \tilde{s}_0 \rightarrow s}} \rho^i d\bar{E}_m(P_0) = \bar{I}_m^\ell \quad (20)$$

should exist. Thus, \bar{I}_m^ℓ can be related to $d\bar{P}_m(Q')$ by [3]

$$\bar{I}_m^\ell = d\bar{P}_m(Q') \cdot \bar{I}_m^\ell \quad (21)$$



$$\begin{aligned}
 \hat{n} \cdot \hat{s} &= \cos \theta^i \\
 \hat{s} &= \hat{n} \cos \theta^i + \hat{t}_j \sin \theta^i \\
 \hat{b}_j &= \hat{t}_j \times \hat{n} = \hat{b} = \hat{s} \times \hat{n}
 \end{aligned}$$

(b)

Figure 5. Ray tube and ray coordinates.

Equations (19)-(21) are, then, combined to yield

$$d\bar{E}_e^m(P_L) \sim d\bar{P}_m(Q') \cdot \bar{T}_m^{\ell} \cdot \frac{e^{-jks}}{s} + O[m_\ell^{-2}, m_\ell^{-3}, \dots] \quad (22)$$

$$\bar{T}_m^{\ell} = \frac{-jk}{4\pi} [\hat{b}_\ell' \hat{n} A + \hat{t}_\ell' \hat{b} B + \hat{b}_\ell' \hat{b} C + \hat{t}_\ell' \hat{n} D] \quad (23)$$

$$\bar{T}_e^{\ell} = \frac{-jkZ_0}{4\pi} [\hat{n}' \hat{n} M + \hat{n}' \hat{b} N] \quad (24)$$

with A, B, C, D, M, and N are defined in Table 2. Note that $d\bar{E}_e^m(P_L)$ is decoupled into \hat{n} and \hat{b} components as follows:

(a) $d\bar{P}_m(Q')$ case:

$$d\bar{E}_m^{\hat{n}}(P_L) = \frac{-jk}{4\pi} [(d\bar{P}_m \cdot \hat{b}') (H^\ell + T_0^2 F \cos \theta^i) + (d\bar{P}_m \cdot \hat{t}') T_0 F \cos \theta^i] \frac{e^{-jks}}{s} + O[m_\ell^{-2}] \quad (25)$$

$$d\bar{E}_m^{\hat{b}}(P_L) = \frac{-jk}{4\pi} [(d\bar{P}_m \cdot \hat{b}') T_0 F + (d\bar{P}_m \cdot \hat{t}') (S^\ell - T_0^2 F \cos^2 \theta^i)] \frac{e^{-jks}}{s} + O[m_\ell^{-2}, m_\ell^{-3}] \quad (26)$$

(b) $d\bar{P}_e(Q')$ case:

$$dE_e^n(p_L) = \frac{-jkZ_0}{4\pi} dP_e(Q') \sin \theta^i [H^L + T_c^2 F \cos \theta^i] \frac{e^{-jks}}{s} + O[m_\ell^{-2}] \quad (27)$$

$$dE_e^b(p_L) = \frac{-jkZ_0}{4\pi} dP_e(Q') \sin \theta^i T_o F \frac{e^{-jks}}{s} + O[m_\ell^{-2}] \quad (28)$$

where

$$H^L = g(\xi_\ell) e^{-j\xi_\ell^3/3} \quad (29)$$

$$S^L = \frac{-j}{m_\ell(Q')} \tilde{g}(\xi_\ell) e^{-j\xi_\ell^3/3} \quad (30)$$

and

$$\xi_\ell = -m_\ell(Q') \cos \theta^i \quad (31)$$

$$m_\ell(Q') = \frac{m(Q')}{(1+T_o^2 \cos^2 \theta^i)^{1/3}} \quad (32)$$

The angle θ^i is defined by $\hat{n}' \cdot \hat{s} = \cos \theta^i$ as shown in Figure 5. Also,

$$F = \frac{S^L - H^L \cos \theta^i}{1+T_o^2 \cos^2 \theta^i} \quad (33)$$

as defined in Table II.

TABLE II
(FOR LIT REGION)

SLOT OR $\epsilon \hat{z}_0$ CASE				MONOPOLE OR $\epsilon \hat{z}_0$ CASE		T_0	F
A	B	C	D	M	N		
$u^2 + \tau_0^2 F \cos \theta'$	$u^2 - \tau_0^2 F \cos \theta'$	$\tau_0 F$	$\tau_0 F \cos \theta'$	$\sin \theta' [u^2 + \tau_0^2 F \cos \theta']$	$\sin \theta' \tau_0 F$	$T(\theta') P_0(\theta')$	$\frac{u^2 - u^2 \cos \theta'}{1 + \tau_0^2 \cos \theta'}$

D. Pattern Factors

The solutions for short magnetic or electric dipoles have been given in part (B) and (C). One approach to analyze an extended aperture or linear antenna problem is to integrate the above solutions over the source distribution, if it is known. This is an application of the superposition theorem, and one approximates the source distribution by an array of short magnetic (or electric) dipoles on the conducting surface. This is an accurate solution, however, rather tedious. A more efficient approach is to modify $\bar{d}^m_e(\theta')$ as shown in Reference [6] such that

(a) in the shadow region:

$$\bar{p}_m = \hat{p}_m \frac{2B}{\pi} \left[\frac{\cos(\frac{kB}{2}(\hat{p}_m \cdot \hat{t}'))}{1 - (\frac{kB}{\pi}(\hat{p}_m \cdot \hat{t}'))^2} \right] \left[\frac{\sin(\frac{kA}{2} \hat{p}_m \cdot \hat{b}')}{\frac{kA}{2} \hat{p}_m \cdot \hat{b}'} \right]$$

$$\bar{p}_e = \hat{n}' [1 - \cos(kL)] \quad (35)$$

(b) in the lit region:

$$\bar{p}_m = \hat{p}_m \frac{2B}{\pi} \left[\frac{\cos(\frac{kB}{2} \sin \theta^i (\hat{p}_m \cdot \hat{t}'))}{1 - (\frac{kB}{\pi} \sin \theta^i (\hat{p}_m \cdot \hat{t}'))^2} \right] \left[\frac{\sin(\frac{kA}{2} \sin \theta^i \hat{p}_m \cdot \hat{b}')}{\frac{kA}{2} \sin \theta^i (\hat{p}_m \cdot \hat{b}')} \right] \quad (36)$$

$$\bar{p}_e = \hat{n}' \frac{\cos(kL \hat{n}' \cdot \hat{s}) - \cos(kL)}{1 - (\hat{n}' \cdot \hat{s})^2} \quad (37)$$

Here \hat{p}_m = unit vector in the direction of magnetic current moment,

A, B = the length of the short and long sides of the slot, and

L = the length of the monopole.

It is noted that L is not to exceed a quarter wavelength for the solutions to be valid.

E. Ellipsoid Surface Parameters

The formulations in section (B)-(D) are used to solve for the radiated fields of antennas mounted on an ellipsoid. Using the ellipsoid geometry shown in Figure 6, the surface is defined by

$$\begin{aligned} \vec{R}(\theta, \phi) = & R(\theta, \phi) \sin \theta \cos \phi \hat{x} + R(\theta, \phi) \sin \theta \sin \phi \hat{y} \\ & + R(\theta, \phi) \cos \theta \hat{z} \end{aligned} \quad (38)$$

or,

$$\vec{R}(V_e, V_r) = a \cos V_e \cos V_r \hat{x} + b \cos V_e \sin V_r \hat{y} + c \sin V_e \hat{z} \quad (39)$$

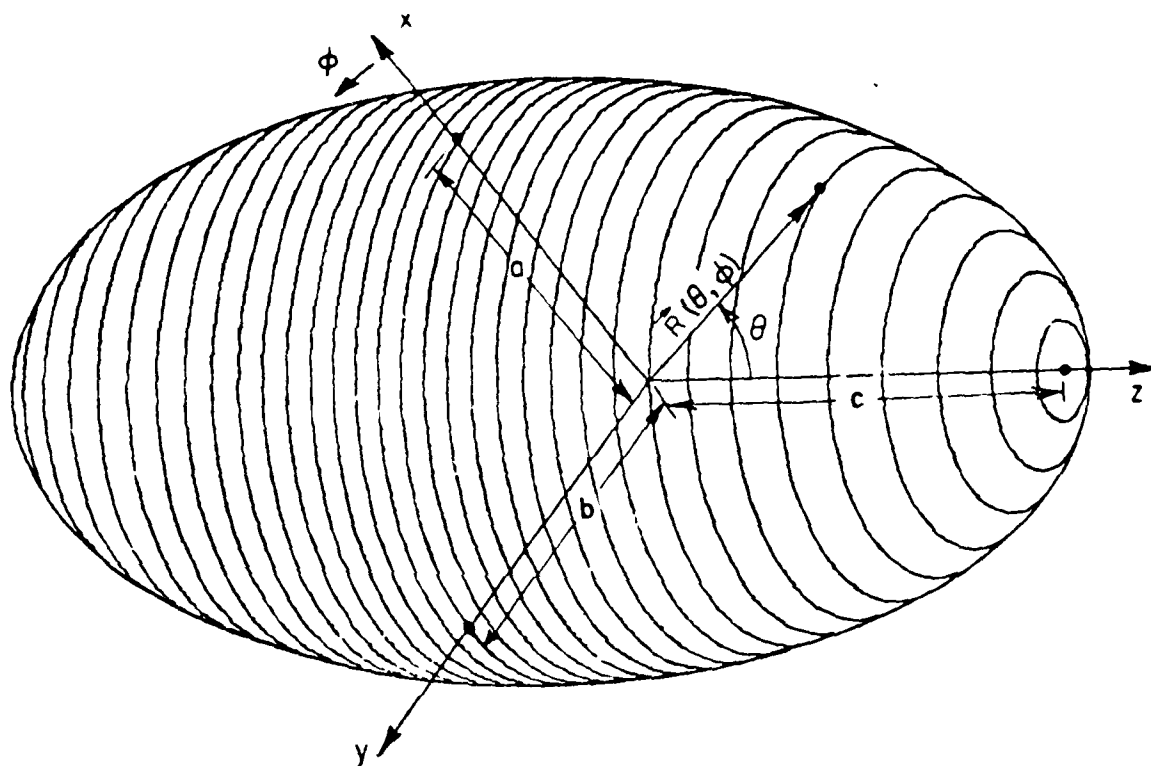


Figure 6. Geometry of an ellipsoid.

with

$$\tan V_e = \frac{a \cos \theta}{c \sin \theta} \quad \text{and} \quad \tan V_r = \frac{a \sin \phi}{b \cos \phi} \quad . \quad (40)$$

The V_r and V_e parameters are introduced because of those convenience in analyzing elliptic geometries.

Considering a ray which propagates along a geodesic path $Q'Q$ on the ellipsoid surface as shown in Figure 7, the three unit vectors \hat{t} , \hat{n} , and \hat{b} are, as defined earlier, the geodesic tangent, outward surface normal and binormal at any point along the geodesic path. The outward surface unit normal (\hat{n}) is obtained from

$$\hat{n} = \frac{\vec{R}_{V_r} \times \vec{R}_{V_e}}{|\vec{R}_{V_r} \times \vec{R}_{V_e}|} \quad (41)$$

where

$$\vec{R}_{V_e} = \frac{\partial \vec{R}}{\partial V_e} = -a \sin V_e \cos V_r \hat{x} - b \sin V_e \sin V_r \hat{y} + c \cos V_e \hat{z}$$

and

$$\vec{R}_{V_r} = \frac{\partial \vec{R}}{\partial V_r} = -a \cos V_e \sin V_r \hat{x} + b \cos V_e \cos V_r \hat{y} \quad .$$

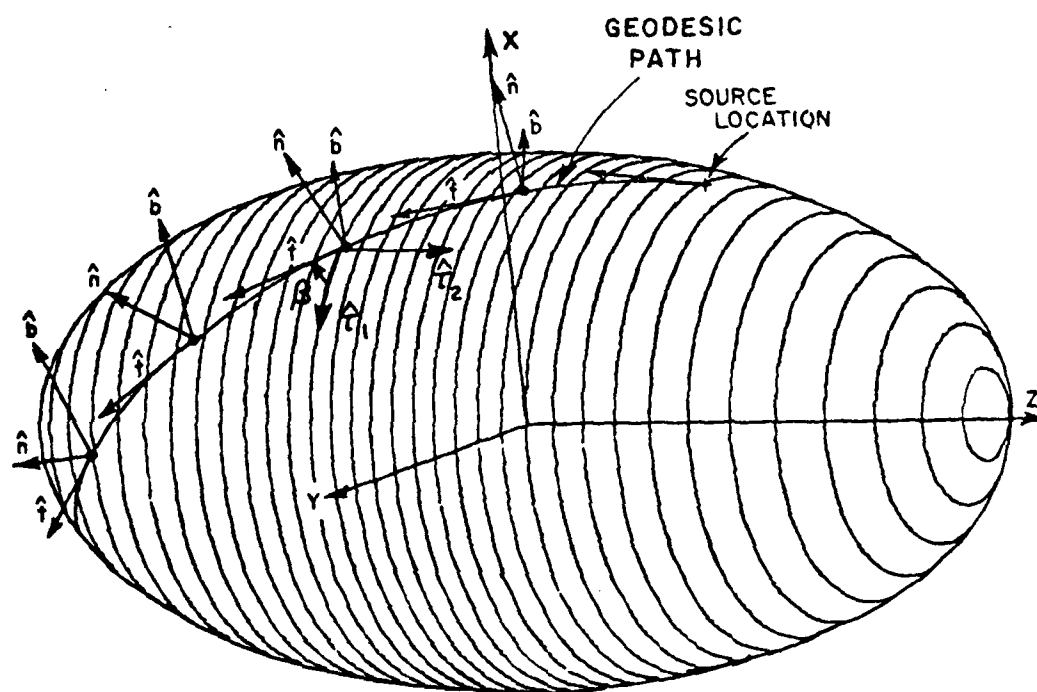


Figure 7. Geodesic path on an ellipsoid.

Then,

$$\hat{n} = \frac{bc \cos^2 V_e \cos V_r \hat{x} + ac \cos^2 V_e \sin V_r \hat{y} + ab \cos V_e \sin V_e \hat{z}}{[b^2 c^2 \cos^4 V_e \cos^2 V_r + a^2 c^2 \cos^4 V_e \sin^2 V_r + a^2 b^2 \cos^2 V_e \sin^2 V_e]^{1/2}}$$

$$= \frac{\frac{\cos V_e \cos V_r}{a} \hat{x} + \frac{\cos V_e \sin V_r}{b} \hat{y} + \frac{\sin V_e}{c} \hat{z}}{A} \quad (42)$$

$$\text{where } A = \left[\left(\frac{\cos V_e \cos V_r}{a} \right)^2 + \left(\frac{\cos V_e \sin V_r}{b} \right)^2 + \left(\frac{\sin V_e}{c} \right)^2 \right]^{1/2} \quad (43)$$

The normal curvatures K_n on the surface are evaluated by introducing the first and second fundamental forms of differential geometry [5] such that

$$K_n = \frac{L dV_r^2 + 2M dV_r dV_e + N dV_e^2}{E dV_r^2 + 2F dV_r dV_e + G dV_e^2} \quad (44)$$

where

$$L = \vec{R}_{VrVr} \cdot \hat{N}, \quad M = \vec{R}_{VrVe} \cdot \hat{N}, \quad N = \vec{R}_{VeVe} \cdot \hat{N}$$

$$E = \vec{R}_{Vr} \cdot \vec{R}_{Vr}, \quad F = \vec{R}_{Vr} \cdot \vec{R}_{Ve}, \quad G = \vec{R}_{Ve} \cdot \vec{R}_{Ve}$$

and $\hat{N} = -\hat{n}$.

It can be shown that

$$\vec{R}_{V_e V_e} = -a \cos V_e \cos V_r \hat{x} - b \cos V_e \sin V_r \hat{y} - c \sin V_e \hat{z}$$

$$\vec{R}_{V_e V_r} = a \sin V_e \sin V_r \hat{x} - b \sin V_e \cos V_r \hat{y}$$

$$\vec{R}_{V_r V_r} = -a \cos V_e \cos V_r \hat{x} - b \cos V_e \sin V_r \hat{y} .$$

After some algebraic manipulation, one obtains

$$L = \frac{\cos^2 V_e}{A}$$

$$M = 0$$

$$N = \frac{1}{A}$$

$$E = a^2 \cos^2 V_e \sin^2 V_r + b^2 \cos^2 V_e \cos^2 V_r$$

$$F = (a^2 - b^2) \sin^2 V_e \sin^2 V_r$$

$$G = a^2 \sin^2 V_e \cos^2 V_r + b^2 \sin^2 V_e \sin^2 V_r + c^2 \cos^2 V_e$$

A pair of orthogonal directions exists for which curvature, K , assumes maximum and minimum values, i.e., principal directions represented by two unit vectors \hat{r}_1 and \hat{r}_2 . Two extreme values of K corresponding to the above directions are called principal curvatures denoted by K_1 and K_2 .

$$\text{Mean curvature: } K_M = \frac{K_1 + K_2}{2} = \frac{EN - 2MF + LG}{2(EG - F^2)}$$

$$\text{Gaussian curvature: } K_G = K_1 K_2 = \frac{LN - M^2}{EG - F^2}$$

Thus, the principal curvatures K_1 and K_2 are given by

$$K_{1,2} = K_M \pm \sqrt{K_M^2 - K_G} \quad (45)$$

The two principal directions $(\hat{\tau}_1, \hat{\tau}_2)$ are given by

$$\begin{aligned} \hat{\tau}_1 &= \frac{1}{\gamma_1} \left[1 \vec{R}_{V_r} + \alpha \vec{R}_{V_e} \right] \\ \hat{\tau}_2 &= \frac{1}{\gamma_2} \left[\beta \vec{R}_{V_r} + 1 \vec{R}_{V_e} \right] \end{aligned} \quad (46)$$

where

$$\alpha = \frac{L - K_1 E}{K_1 F - M}, \quad \beta = \frac{M - K_2 F}{K_2 E - L}$$

$$\gamma_1 = (E + 2\alpha F + \alpha^2 G)^{1/2}, \quad \gamma_2 = (\beta^2 E + 2\beta F + G)^{1/2} \quad (47)$$

However, it is noticed that $K_1 \sim L/E$ and $K_2 \sim N/G$ within the significant energy region for most practical cases. That indicates approximate values of the two principal curvatures, $K_1 \sim L/E$ and $K_2 \sim N/G$, are good enough to be used for the geodesics on the ellipsoid surface for our radiation consideration.

Thus

$$\begin{aligned}
 K_1 &\approx \frac{L}{E} \\
 &= \frac{\cos^2 V_e}{A [a^2 \cos^2 V_e \sin^2 V_r + b^2 \cos^2 V_e \cos^2 V_r]} \\
 &= (A[a^2 \sin^2 V_r + b^2 \cos^2 V_r])^{-1}
 \end{aligned} \tag{48}$$

$$\begin{aligned}
 K_2 &\approx \frac{N}{G} \\
 &= \frac{1}{A [a^2 \sin^2 V_e \cos^2 V_r + b^2 \sin^2 V_e \sin^2 V_r + c^2 \cos^2 V_e]} .
 \end{aligned} \tag{49}$$

It is noticed that $R_1 = \frac{1}{K_1}$ and $R_2 = \frac{1}{K_2}$ as found in Table I. For most practical cases, α and β within the significant energy region become very small. Thus, one may use R_{V_r} and R_{V_e} as the principal surface

directions, which are expressed by $\hat{\tau}_1, \hat{\tau}_2$, respectively.

If β' denotes the angle between \hat{t} and $\hat{\tau}_1$, then $\hat{t} = \hat{\tau}_1 \cos \beta' + \hat{\tau}_2 \sin \beta'$.

From Euler's theorem, the normal curvature along the geodesic path is specified by

$$K_g = K_1 \cos^2 \beta' + K_2 \sin^2 \beta' \quad (50)$$

with the radius of curvature, ρ_g , being $1/K_g$.

The torsion term (T_0) introduced in Section (B) is given by

$$T_0 = T \cdot \rho_g \quad (51)$$

where the surface torsion is given by

$$T = \frac{\sin 2 \beta'}{2} (K_2 - K_1) \quad (52)$$

with K_1 and K_2 being defined in Equations (48) and (49).

CHAPTER III

NUMERICAL TECHNIQUE AND PERTURBATION METHOD

A. Introduction

It is seen that, for an antenna mounted on an ellipsoid, the geodesic paths associated with the GTD solution in the shadow region are extremely complex. An elaborate method employed calculus of variations to calculate the geodesic paths which resulted in a very inefficient solution is presented in Chapter IV. An efficient numerical approach is examined in this chapter with the ellipsoid simulated by an elliptic cone

or elliptic cylinder model. Since the elliptic cone and elliptic cylinder are developed surfaces, geodesics are efficient to solve.

B. Surface Geodesics

The geodesics on the elliptic cylinder, elliptic cone and ellipsoid are presented in this section.

a) Elliptic Cylinder Case:

The elliptic cylinder geometry used for this study is shown in Figure 8(a). Since the elliptic cylinder is a developed surface, the geodesic path Q'Q is a straight line on the unfolded planar surface. As shown in Figure 8(b), the geodesic unit tangent \hat{t} is given by

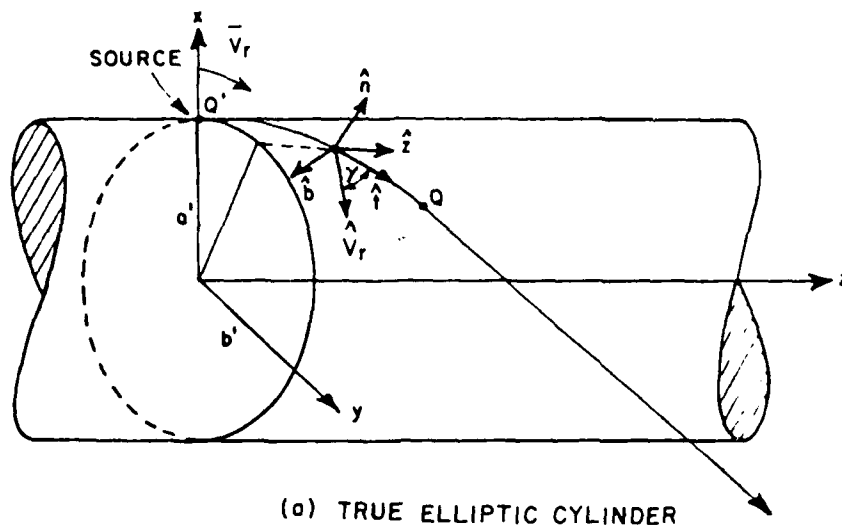
$$\hat{t} = \hat{V}_r \cos \gamma + \hat{z} \sin \gamma \quad (53)$$

$$\text{where } \hat{V}_r = \frac{-a \sin V_r \hat{x} + b \cos V_r \hat{y}}{(a^2 \sin^2 V_r + b^2 \cos^2 V_r)^{1/2}} \quad (54)$$

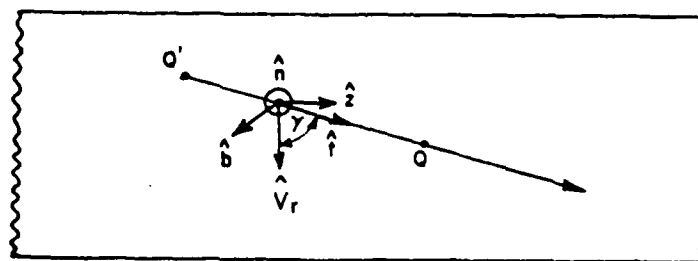
It is noticed that \hat{V}_r and \hat{z} are the two principal directions on the elliptic cylinder surface. For a given geodesic Q'Q, one can see that γ is a constant along the geodesic path.

b) Elliptic Cone Case:

Consider a ray propagates along a geodesic path Q'Q on the elliptic cone surface as shown in Figure 9(a). It is a straight line on the unfolded planar surface as shown in Figure 9(b). It is noticed that \hat{V}_r and \hat{t}_e are the two principal directions on the surface. The geodesic



(a) TRUE ELLIPTIC CYLINDER



(b) UNFOLDED PLANAR SURFACE

Figure 8. Geodesic path on a developed elliptic cylinder.

unit tangent \hat{t} is, then, represented by

$$\hat{t} = \hat{t}_r \cos \beta + \hat{t}_e \sin \beta \quad (55)$$

where

$$\hat{t}_e = -\hat{x}_e \sin \delta + \hat{z} \cos \delta \quad (56)$$

$$\hat{x}_e = \frac{\hat{x} a' \cos V_r + \hat{y} b' \sin V_r}{\sqrt{a'^2 \cos^2 V_r + b'^2 \sin^2 V_r}} \quad (57)$$

and δ is the half cone angle as shown in Figure 9(a). Note that β is no longer a constant along the geodesic path $Q'Q$.

(c) Ellipsoid Case:

Recall that the ellipsoid surface is defined by

$$\vec{R}(V_e, V_r) = a \cos V_e \cos V_r \hat{x} + b \cos V_e \sin V_r \hat{y} + c \sin V_e \hat{z}$$

with

$$\tan V_e = \frac{a \cos \theta}{c \sin \theta}$$

and

$$\tan V_r = \frac{a \sin \phi}{b \cos \phi} \quad .$$

From Section II-(E), it was found that the principal directions were given by \vec{R}_{V_e} and \vec{R}_{V_r} . As shown in Figures 10(a) and (b) the unit vectors in the principal directions can be represented by

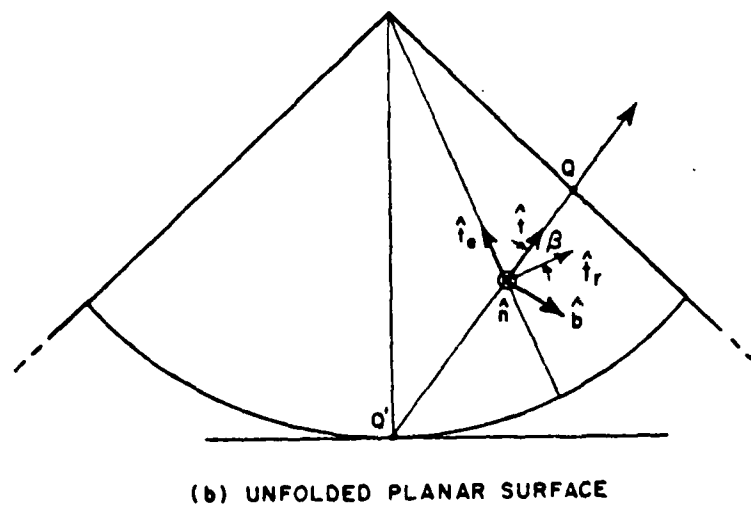
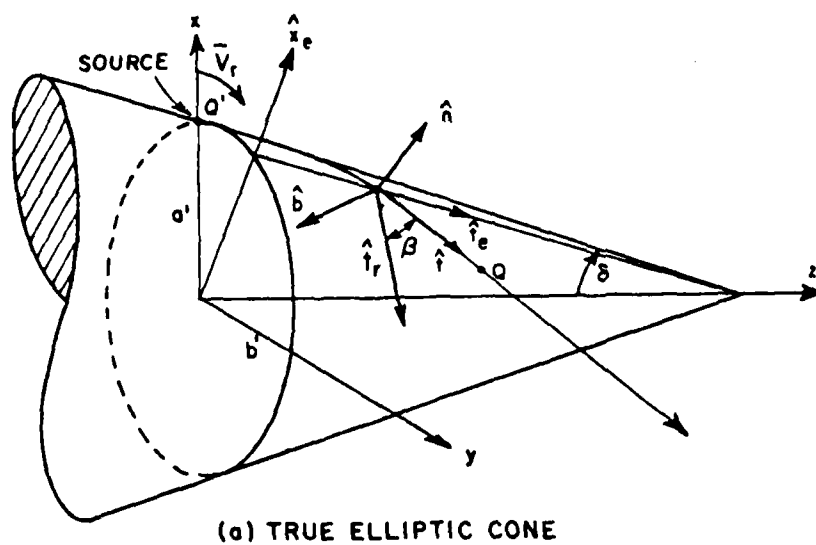


Figure 9. Geodesic path on a developed elliptic cone.

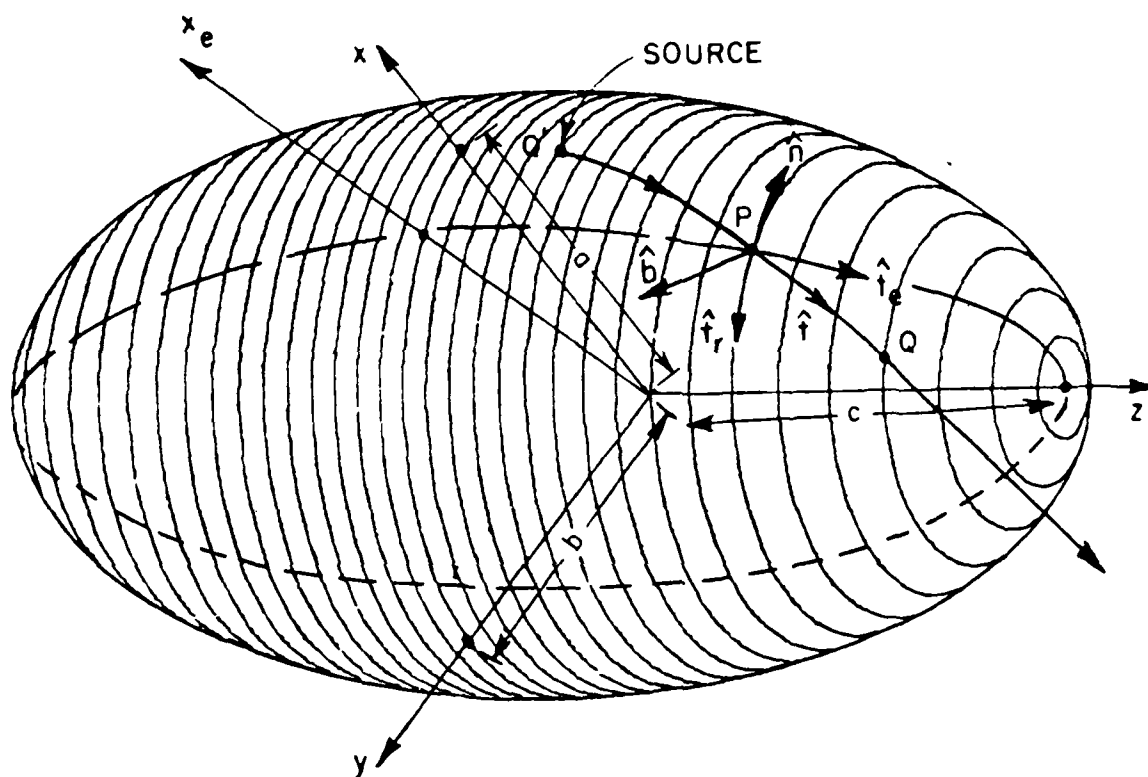
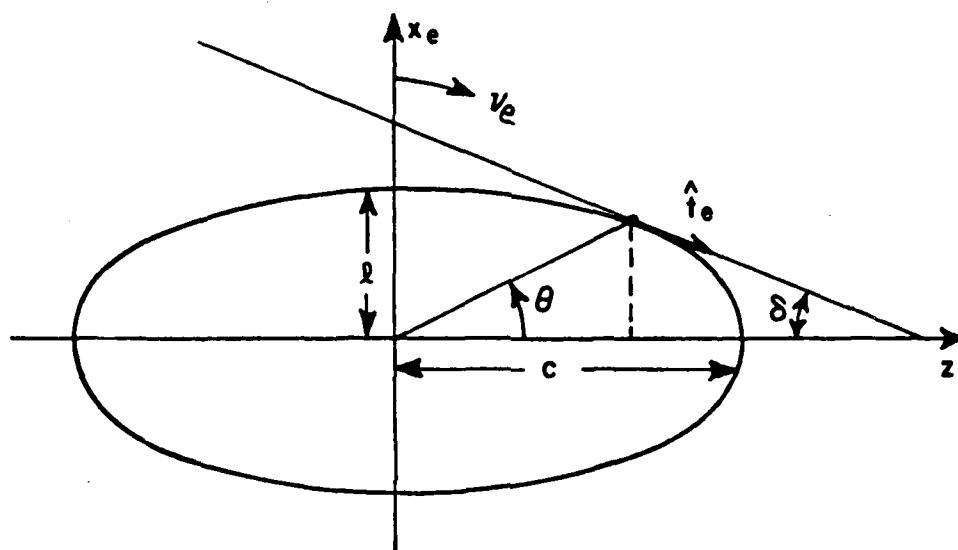


Figure 10(a). Geodesic path on an ellipsoid.



$$l = \sqrt{a^2 \cos^2 V_r + b^2 \sin^2 V_r}$$

Figure 10(b). Elliptic profile.

$$\hat{t}_r \sim \vec{R}_{V_r} / |\vec{R}_{V_r}|$$

$$\sim \frac{-a \cos V_e \sin V_r \hat{x} + b \cos V_e \cos V_r \hat{y}}{\sqrt{a^2 \cos^2 V_e \sin^2 V_r + b^2 \cos^2 V_e \cos^2 V_r}} \quad (58)$$

$$\hat{t}_e \sim \vec{R}_{V_e} / |\vec{R}_{V_e}|$$

$$\sim \frac{-a \sin V_e \cos V_r \hat{x} - b \sin V_e \sin V_r \hat{y} + c \cos V_e \hat{z}}{\sqrt{a^2 \sin^2 V_e \cos^2 V_r + b^2 \sin^2 V_e \sin^2 V_r + c^2 \cos^2 V_e}} \quad (59)$$

If β denotes the angle between \hat{t}_r and the geodesic unit tangent \hat{t} , then

$$\hat{t} = \hat{t}_r \cos \beta + \hat{t}_e \sin \beta \quad (60)$$

which is identical to the form used for the elliptic cylinder and elliptic cone geodesics. This suggests that one might be able to develop a perturbation solution which gives a simplified form for β on an ellipsoid using the elliptic cylinder or elliptic cone expressions for β .

C. Elliptic Cylinder Perturbation

In order to solve for the geodesics on an ellipsoid, the elliptic cylinder perturbation technique is used when the source is located at $\theta_s = 90^\circ$. Note that the source position is assumed to be in the $\phi_s = 0$ plane.

Recalling that γ is a constant along a given geodesic path on an elliptic cylinder, one obtains a geodesic equation given by

$$\tan \gamma = \frac{S_e}{S_r} \quad . \quad (61)$$

The elliptic cross-section in the $x_e - z$ plane is described by

$$x_e = \sqrt{a^2 \cos^2 V_r + b^2 \sin^2 V_r} \cos V_e$$

$$z = c \sin V_e$$

therefore,

$$\begin{aligned} S_e &= \int_0^{V_e} \sqrt{\left(\frac{dx_e}{dV_e}\right)^2 + \left(\frac{dz}{dV_e}\right)^2} dV_e' \\ &= \int_0^{V_e} \sqrt{(a^2 \cos^2 V_r + b^2 \sin^2 V_r) \sin^2 V_e' + c^2 \cos^2 V_e'} dV_e' \quad . \end{aligned} \quad (62)$$

The elliptic cross-section in the $x'-y'$ plane is described by

$$x' = a \cos V_e \cos V_r$$

$$y' = b \cos V_e \sin V_r$$

therefore,

$$\begin{aligned}
 S_r &= \int_0^{V_r} \sqrt{\left(\frac{dx}{dV_r'}\right)^2 + \left(\frac{dy}{dV_r'}\right)^2} dV_r' \\
 &= \int_0^{V_r} \sqrt{a^2 \cos^2 V_e \sin^2 V_r' + b^2 \cos^2 V_e \cos^2 V_r'} dV_r' \quad .
 \end{aligned}
 \tag{63}$$

Thus, Equation (61) becomes

$$\begin{aligned}
 \tan \gamma &= \frac{\int_0^{V_e} \sqrt{(a^2 \cos^2 V_r + b^2 \sin^2 V_r) \sin^2 V_e' + c^2 \cos^2 V_e'} dV_e'}{\int_0^{V_r} \sqrt{a^2 \cos^2 V_e \sin^2 V_r' + b^2 \cos^2 V_e \cos^2 V_r'} dV_r'} \quad .
 \end{aligned}
 \tag{64}$$

At the diffraction point Q, the radiation direction (θ_t, ϕ_t) should coincide with the geodesic tangent \hat{t} given in Equation (60). Thus,

$$\begin{aligned}
 \hat{t} &= \hat{x} \sin \theta_t \cos \phi_t + \hat{y} \sin \theta_t \sin \phi_t + \hat{z} \cos \theta_t \\
 &= \hat{t}_r \cos \gamma + \hat{t}_e \sin \gamma
 \end{aligned}
 \tag{65}$$

In order to trace the geodesic path from the source location to the diffraction point, one can always assume a diffraction point at the source $(V_e, V_r) = (0,0)$ with the radiation direction $(\theta_t, \pm \frac{\pi}{2})$ and gradually add increments $(\Delta\theta_t, \Delta\phi_t)$ until the desired radiation direction (θ_t, ϕ_t) is reached.

After the geodesic path is determined, it is necessary to check the significant energy region by calculating the Fock parameter. The Fock parameter ξ of Equation (12) is given by

$$\xi = \int_{Q'}^Q \frac{1}{\rho_g} \left(\frac{k \rho_g}{2} \right)^{1/3} dl, \quad (66)$$

where the integral is evaluated along the geodesic path. Note that l is the arc length along the geodesic and given by either of the following equations;

$$l = \frac{S_e}{\sin \gamma} \quad \text{or} \quad l = \frac{S_r}{\cos \gamma}.$$

Therefore

$$dl = \frac{1}{\sin \gamma} \sqrt{(a^2 \cos^2 v_r + b^2 \sin^2 v_r) \sin^2 v_e + c^2 \cos^2 v_e} dv_e$$

or,

$$dl = \frac{1}{\cos \gamma} \sqrt{a^2 \cos^2 v_e \sin^2 v_r + b^2 \cos^2 v_e \cos^2 v_r} dv_r$$

and the integration can be written as

$$\xi = \frac{1}{\sin \gamma} \int_0^{v_e} \frac{1}{\rho_g} \left(\frac{k \rho_g}{2} \right)^{1/3} \sqrt{(a^2 \cos^2 v_r + b^2 \sin^2 v_r) \sin^2 v'_e + c^2 \cos^2 v'_e} dv'_e \quad (67)$$

or

$$= \frac{1}{\cos \gamma} \int_0^{V_r} \frac{1}{\rho g} \left(\frac{k \rho g}{2} \right)^{\frac{1}{3}} dV_r' \quad (68)$$

$$\sqrt{a^2 \cos^2 V_e \sin^2 V_r' + b^2 \cos^2 V_e \cos^2 V_r'} dV_r'.$$

where $\rho g = 1 / (k_1 \cos^2 \gamma + k_2 \sin^2 \gamma)$ and k_1, k_2 are given in Equations (48) and (49).

D. Elliptic Cone Perturbation

When the source is not located at the mid-section ($\theta_s \neq 90^\circ$), the elliptic cone perturbation method is used. The geodesic path on an ellipsoid using the elliptic cone perturbation method is shown in Figure 11 and the associated unfolded surface is shown in Figure 12. If γ and β denote the angle between \hat{t} and \hat{t}_r at Q' and Q respectively, it is seen in Section III-(B) that they are not the same as in the elliptic cylinder case.

In fact,

$$\beta = \gamma - \alpha \quad (69)$$

The calculation of α will be discussed in detail in this section.

$$\vec{r} = \hat{x} a \cos V_{es} \cos V_{rs} + \hat{y} b \cos V_{es} \sin V_{rs} + \hat{z} c \sin V_{es}$$

$$\vec{t}_e = \frac{\partial \vec{r}}{\partial V_{es}} = -\hat{x} a \sin V_{es} \cos V_{rs} - \hat{y} b \sin V_{es} \sin V_{rs} + \hat{z} c \cos V_{es}$$

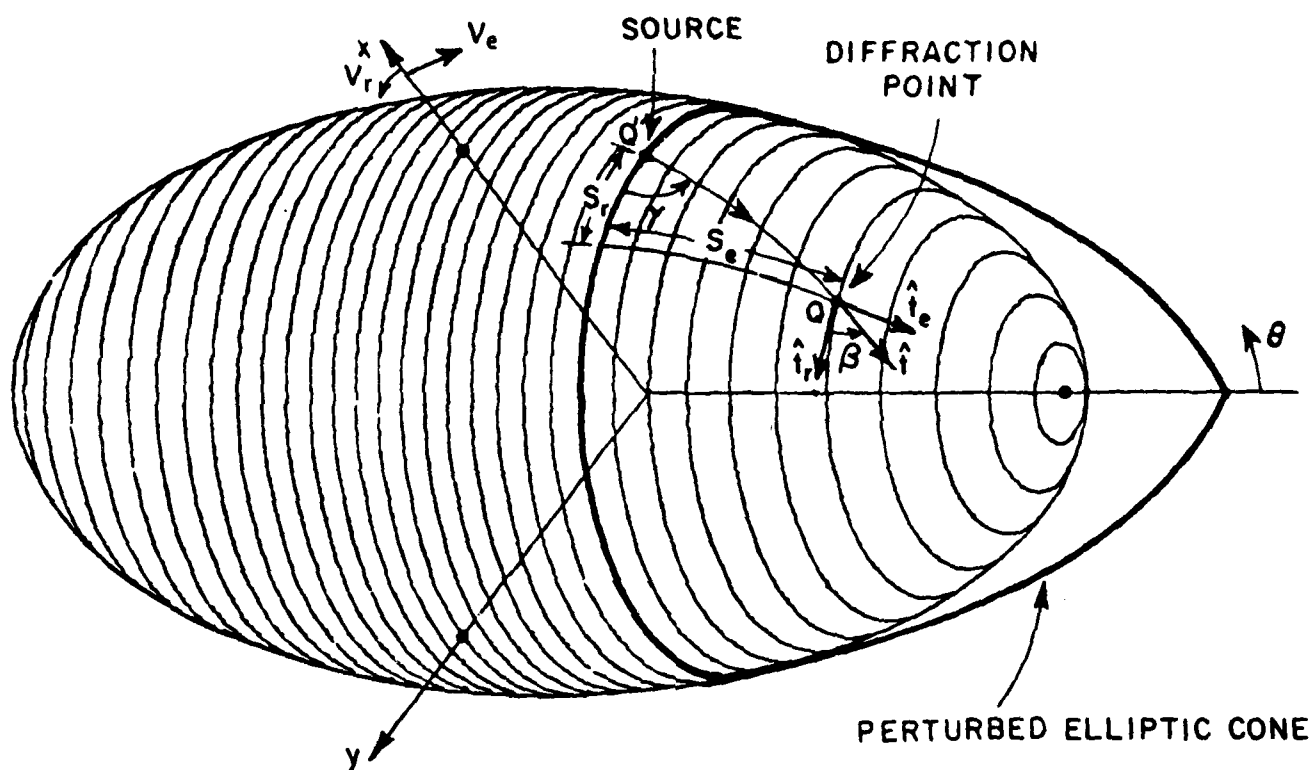


Figure 11. Geodesic path on the perturbed elliptic cone.

therefore, one can show that

$$\frac{x-a \cos V_{es} \cos V_{rs}}{-a \sin V_{es} \cos V_{rs}} = \frac{y-b \cos V_{es} \sin V_{rs}}{-b \sin V_{es} \sin V_{rs}} = \frac{z-c \sin V_{es}}{c \cos V_{es}} .$$

For $x = y = 0$, $z = c \csc V_{es}$.

Accordingly,

$$\begin{aligned} r_s &= [a^2 \cos^2 V_{es} \cos^2 V_{rs} + b^2 \cos^2 V_{es} \sin^2 V_{rs} \\ &\quad + (c \sin V_{es} - c \csc V_{es})^2]^{1/2} \\ &= [a_s^2 \cos^2 V_{rs} + b_s^2 \sin^2 V_{rs} + z_s^2 \cot^4 V_{es}]^{1/2} \end{aligned}$$

where $z_s = c \sin V_{es}$

$a_s = a \cos V_{es}$

$b_s = b \cos V_{es}$.

From Figure 13(b) and (c),

$$\vec{l} = \hat{x} a_s \cos V_{rs} + \hat{y} b_s \sin V_{rs} .$$

$$\frac{\partial \vec{l}}{\partial V_{rs}} = -\hat{x} a_s \sin V_{rs} + \hat{y} b_s \cos V_{rs} .$$

From the previous calculation, one can define a new vector \vec{U} as following:

$$\vec{U} = \left(\frac{\partial \vec{l}}{\partial V_{rs}} \right) \times \left(\frac{\partial \vec{r}}{\partial V_{es}} \right)$$

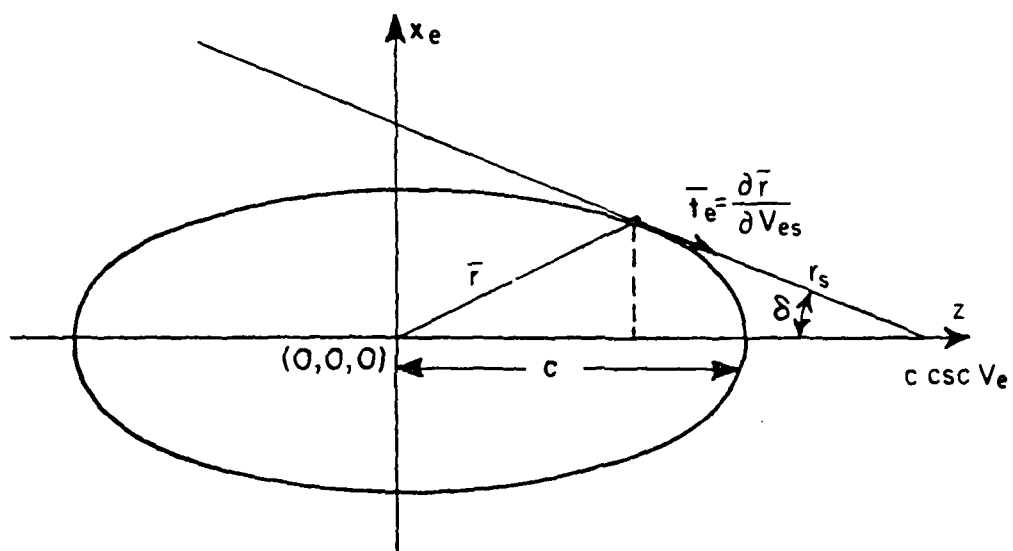


Figure 13(a). Elliptic profile

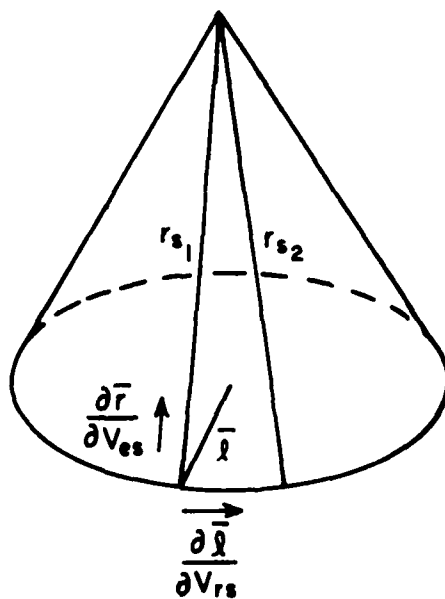


Figure 13(b). Elliptic Cone.

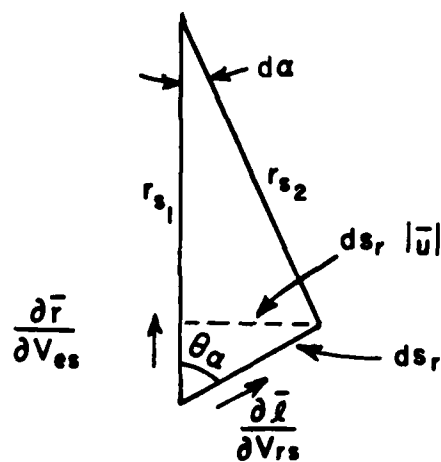


Figure 13(c). Unfolded planar surface of the Elliptic Cone.

$$\begin{aligned}
& + \hat{z} c \cos V_{es}) \\
= & \frac{(-\hat{x} a_s \sin V_{rs} + \hat{y} b_s \cos V_{rs})_x (-\hat{x} a \sin V_{es} \cos V_{rs} - \hat{y} b \sin V_{es} \sin V_{rs} \\
& [a_s^2 \sin^2 V_{rs} + b_s^2 \cos^2 V_{rs}]^{1/2} [a^2 \sin^2 V_{es} \cos^2 V_{rs} + b^2 \sin^2 V_{es} \sin^2 V_{rs} \\
& + c^2 \cos^2 V_{es}]^{1/2}}{ \\
= & \frac{\hat{x} b_s c \cos V_{es} \cos V_{rs} + \hat{y} a_s c \cos V_{es} \sin V_{rs} + \hat{z} a_s b \sin V_{es}}{[a_s^2 \sin^2 V_{rs} + b_s^2 \cos^2 V_{rs}]^{1/2} [a^2 \sin^2 V_{es} \cos^2 V_{rs} + b^2 \sin^2 V_{es} \sin^2 V_{rs} \\
& + c^2 \cos^2 V_{es}]^{1/2}}
\end{aligned}$$

The magnitude of vector \vec{U} becomes

$$\begin{aligned}
|\vec{U}| &= \left(\frac{\partial \vec{r}}{\partial V_{rs}} \right) \left(\frac{\partial \vec{r}}{\partial V_{es}} \right) \sin \theta_R \\
&= \sin \theta_R
\end{aligned}$$

From Figure 13(c), one obtains the following equation;

$$d\alpha = \frac{ds_r |\vec{U}|}{r_s} \quad .$$

Therefore α is given by

$$\alpha = \int_{V_{rs}}^{V_r} \frac{\cos V_{es} [a^2 b^2 \sin^2 V_{es} + c^2 \cos^2 V_{es} (a^2 \sin^2 V_r' + b^2 \cos^2 V_r')]^{1/2}}{r_s [c^2 \cos^2 V_{es} + \sin^2 V_{es} (a^2 \cos^2 V_r' + b^2 \sin^2 V_r')]^{1/2}} dv_r'$$

(70)

$$\text{where } r_s = [a_s^2 \cos^2 V_r' + b_s^2 \sin^2 V_r' + z_s^2 \cot^4 V_{es}]^{1/2}.$$

To obtain a diffraction point (V_e, V_r) for a radiation direction (θ_t, ϕ_t) , one can always assume the first diffraction point is at the source $(V_e, V_r) = (V_s, 0)$ with the radiation direction $(\frac{\pi}{2}, \pm \frac{\pi}{2})$ and gradually add the increments $(\Delta\theta_t, \Delta\phi_t)$ until the final radiation direction (θ_t, ϕ_t) is reached.

The geodesic arc length is obtained from either of the following equations;

$$l \cos \gamma = (r_s - S_e) \sin \alpha, \text{ or} \quad (71)$$

$$l \sin \gamma = r - (r_s - S_e) \cos \alpha. \quad (72)$$

Therefore

$$dl = \frac{r \cos \gamma}{\cos^2(\gamma - \alpha)} d\alpha, \text{ or}$$

$$dl = - \frac{1}{\sin(\gamma - \alpha)} \frac{d}{dV_e} (r_s - S_e) \cdot dV_e.$$

The Fock parameter ξ is obtained by integrating along V_r or V_e , i.e.,

$$\begin{aligned} \xi &= r \cos \gamma \int_0^\alpha \frac{1}{\rho_g} \left(\frac{k \rho_g}{2} \right)^{\frac{1}{3}} \frac{1}{\cos^2(\gamma - \alpha')} d\alpha' \\ &= r \cos \gamma \int_0^{V_r} \frac{1}{\rho_g} \left(\frac{k \rho_g}{2} \right)^{\frac{1}{3}} \frac{1}{\cos^2(\gamma - \alpha)} \frac{d\alpha}{dV_r} dV_r \end{aligned} \quad (73)$$

where

$$\frac{d\alpha}{dV_{rs}} = \frac{\cos V_{es} [a^2 b^2 \sin^2 V_{es} + c^2 \cos^2 V_{es} (a^2 \sin^2 V_{rs} + b^2 \cos^2 V_{rs})]^{1/2}}{r_s [c^2 \cos^2 V_{es} + \sin^2 V_{es} (a^2 \cos^2 V_{rs} + b^2 \sin^2 V_{rs})]}$$

or

$$\xi = \int_0^{V_e} \frac{-1}{\rho_g} \left(\frac{k \rho_g}{2} \right)^{\frac{1}{3}} \frac{1}{\sin(\gamma - \alpha)} \frac{d}{dV_e} (r_s - s_e) \cdot dV_e \quad (74)$$

$$\text{where } \rho_g = \frac{1}{K_1 \cos^2 \gamma + K_2 \sin^2 \gamma} \quad \text{and}$$

K_1, K_2 are given in Equations (48) and (49).

CHAPTER IV

EXACT GEODESIC PATHS OF AN ELLIPSOID

More elaborate numerical method employing calculus of variations to calculate the geodesic paths on an ellipsoid is studied in this chapter in order to check the validity of the previous perturbation solutions.

Using rectangular coordinates, an ellipsoid can be described by

$$\frac{x^2}{a^2} + \frac{y^2}{b^2} + \frac{z^2}{c^2} = 1 \quad (75)$$

where, without loss of generality, it is assumed that $c > b > a > 0$.

The key to the derivation of the geodesic path solution of an ellipsoid is to find a coordinate system which is orthogonal on the ellipsoidal surface.

Consider the following three equations:

$$\frac{x^2}{a^2-\xi} + \frac{y^2}{b^2-\xi} + \frac{z^2}{c^2-\xi} = 1, \quad a^2 > \xi \quad (76)$$

$$\frac{x^2}{a^2-\eta} + \frac{y^2}{b^2-\eta} + \frac{z^2}{c^2-\eta} = 1, \quad b^2 > \eta > a^2 \quad (77)$$

$$\frac{x^2}{a^2-\tau} + \frac{y^2}{b^2-\tau} + \frac{z^2}{c^2-\tau} = 1, \quad c^2 > \tau > b^2 \quad (78)$$

which are respectively of an ellipsoid, a hyperboloid of one sheet and a hyperboloid of two sheets, all confocal with the ellipsoid of Equation (76). The variables $u^1 = \xi$, $u^2 = \eta$, $u^3 = \tau$ are called ellipsoidal coordinates. The transformation to the rectangular coordinates is obtained by solving Equations (76), (77), and (78)

simultaneously for x , y and z , such that

$$x = \pm \left[\frac{(a^2-\xi)(a^2-\eta)(a^2-\tau)}{(c^2-a^2)(b^2-a^2)} \right]^{1/2} \quad (79a)$$

$$y = \pm \left[\frac{(b^2-\xi)(b^2-\eta)(b^2-\tau)}{(c^2-b^2)(a^2-b^2)} \right]^{1/2} \quad (79b)$$

$$z = \pm \left[\frac{(c^2-\xi)(c^2-\eta)(c^2-\tau)}{(a^2-c^2)(b^2-c^2)} \right]^{1/2} \quad (79c)$$

In terms of the ellipsoidal coordinates, the displacement vector $d\vec{r}$ can be written as

$$\begin{aligned}
\vec{dr} &= \frac{\partial \vec{r}}{\partial u^1} du^1 + \frac{\partial \vec{r}}{\partial u^2} du^2 + \frac{\partial \vec{r}}{\partial u^3} du^3 \\
&= \vec{a}_1 du^1 + \vec{a}_2 du^2 + \vec{a}_3 du^3
\end{aligned} \tag{80}$$

Then the length of a line element, denoted by ds , is

$$\begin{aligned}
(ds)^2 &= \vec{dr} \cdot \vec{dr} = \sum_{i=1}^3 \sum_{j=1}^3 \vec{a}_i \cdot \vec{a}_j du^i du^j \\
&= \sum_{i=1}^3 \sum_{j=1}^3 g_{ij} du^i du^j
\end{aligned} \tag{81}$$

$$\text{where } g_{ij} = \vec{a}_i \cdot \vec{a}_j = \frac{\partial x}{\partial u^i} \frac{\partial x}{\partial u^j} + \frac{\partial y}{\partial u^i} \frac{\partial y}{\partial u^j} + \frac{\partial z}{\partial u^i} \frac{\partial z}{\partial u^j} \tag{82}$$

It can be shown, using Equations (79a), (79b) and (79c), that

$$g_{ij} = 0, \text{ if } i \neq j \tag{83a}$$

$$g_{11} = \frac{1}{4} \frac{(\tau - \xi)(\eta - \xi)}{(a^2 - \xi)(b^2 - \xi)(c^2 - \xi)} \tag{83b}$$

$$g_{22} = \frac{1}{4} \frac{(\xi - \eta)(\tau - \eta)}{(a^2 - \eta)(b^2 - \eta)(c^2 - \eta)} \tag{83c}$$

$$g_{33} = \frac{1}{4} \frac{(\eta - \tau)(\xi - \tau)}{(a^2 - \tau)(b^2 - \tau)(c^2 - \tau)} \tag{83d}$$

By substituting Equations (83a) through (83d) into Equation (81), one obtains

$$(ds)^2 = \frac{1}{4} \left\{ \frac{(\tau-\xi)(\eta-\xi)}{(a^2-\xi)(b^2-\xi)(c^2-\xi)} (d\xi)^2 + \frac{(\xi-\eta)(\tau-\eta)}{(a^2-\eta)(b^2-\eta)(c^2-\eta)} (d\eta)^2 \right. \\ \left. + \frac{(\eta-\tau)(\xi-\tau)}{(a^2-\tau)(b^2-\tau)(c^2-\tau)} (d\tau)^2 \right\} \quad (84)$$

For the ellipsoid of Equation (75), $\xi=d\xi=0$. Then Equation (84) becomes

$$(ds)^2 = \frac{1}{4} (\tau-\eta) \left\{ \frac{\eta(d\eta)^2}{(\eta-a^2)(\eta-b^2)(\eta-c^2)} - \frac{\tau(d\tau)^2}{(\tau-a^2)(\tau-b^2)(\tau-c^2)} \right\} \quad (85)$$

or

$$S = \frac{1}{2} \int (\tau-\eta)^{\frac{1}{2}} \left\{ \frac{\eta \eta'^2}{(\eta-a^2)(\eta-b^2)(\eta-c^2)} - \frac{\tau}{(\tau-a^2)(\tau-b^2)(\tau-c^2)} \right\}^{\frac{1}{2}} d\tau \quad (86)$$

where $\eta' = \frac{d\eta}{d\tau}$ and $d\tau$ is assumed to be positive. Let $h(\eta, \eta', \tau)$ denote

the integrand of Equation (86), i.e.,

$$h = (\tau-\eta)^{\frac{1}{2}} \left\{ \frac{\eta \eta'^2}{(\eta-a^2)(\eta-b^2)(\eta-c^2)} - \frac{\tau}{(\tau-a^2)(\tau-b^2)(\tau-c^2)} \right\}^{\frac{1}{2}} \quad (87)$$

Then using the calculus of variation technique, it can be shown that the geodesic path satisfies

$$\frac{d}{d\tau} \frac{\partial h}{\partial \eta'} - \frac{\partial h}{\partial \eta} = 0 \quad . \quad (88)$$

The next step is to express Equation (88) as a complete differential.

From Equation (87), one obtains

$$\begin{aligned} \frac{d}{d\tau} \frac{\partial h^2}{\partial \eta'} &= \frac{\frac{d}{d\tau} [\eta'(\tau-\eta)]}{\eta'(\tau-\eta)} \frac{\partial h^2}{\partial \eta'} + 2 \frac{\partial h^2}{\partial \eta} \\ &+ \frac{2h^2}{\tau-\eta} \end{aligned} \quad (89)$$

and from Equation (88), one obtains

$$\frac{d}{d\tau} \frac{\partial h^2}{\partial \eta'} = 2 \frac{dh}{d\tau} \frac{\partial h}{\partial \eta'} + \frac{\partial h^2}{\partial \eta} \quad . \quad (90)$$

By substituting Equations (88) and (89) into Equation (90) and rearranging the various terms, one obtains

$$\begin{aligned} \frac{d[\eta'(\tau-\eta)]}{d\tau} \frac{1}{h} \frac{\partial h}{\partial \eta'} + \eta'(\tau-\eta) \frac{1}{h} \frac{d}{d\tau} \frac{\partial h}{\partial \eta'} \\ - \eta'(\tau-\eta) \frac{1}{h^2} \frac{dh}{d\tau} \frac{\partial h}{\partial \eta'} + \eta' = 0 \end{aligned}$$

which can be simplified to

$$\frac{d}{d\tau} \left\{ \eta'(\tau-\eta) \frac{1}{h} \frac{\partial h}{\partial \eta'} + (\eta-b^2) \right\} = 0 \quad . \quad (91)$$

The Equation (88) becomes a complete differential. The derivation of the geodesic path solution is straight forward from Equation (91).

It is obvious that

$$\eta'(\tau-\eta) \frac{1}{h} \frac{\partial h}{\partial \eta} + \eta - b^2 = -\beta \quad (92)$$

where β is a constant.

By combining Equation (87) with Equation (92), one obtains

$$\frac{-\eta(d\eta)^2}{(\eta-a^2)(\eta-b^2)(\eta-c^2)(\eta-b^2+\beta)} = \frac{-\tau(d\tau)^2}{(\tau-a^2)(\tau-b^2)(\tau-c^2)(\tau-b^2+\beta)} \quad (93)$$

Since $c^2 > \tau > b^2 > \eta > a^2$, it is obvious that $\tau-b^2+\beta > 0 > \eta-b^2+\beta$ or $b^2-\eta > \beta > b^2-\tau$.

Equation (93) is the geodesic path solution. However, it is more convenient to make the following changes of variables.

$$\eta = a^2 \sin^2 \phi + b^2 \cos^2 \phi, \text{ and} \quad (94a)$$

$$\tau = b^2 \cos^2 \psi + c^2 \sin^2 \psi. \quad (94b)$$

In terms of ϕ and ψ , the geodesic path solution in Equation (93) can be rewritten as

$$\begin{aligned} & \frac{[b^2 - (b^2-a^2) \sin^2 \phi] (d\phi)^2}{[(c^2-b^2) + (b^2-a^2) \sin^2 \phi][-\beta + (b^2-a^2) \sin^2 \phi]} \\ &= \frac{[b^2 + (c^2-b^2) \sin^2 \psi] (d\psi)^2}{[(b^2-a^2) + (c^2-b^2) \sin^2 \psi][\beta + (c^2-b^2) \sin^2 \psi]} \end{aligned} \quad (95)$$

and in integral form as

$$\begin{aligned}
 & \int_{\phi_1}^{\phi} \left\{ \frac{[b^2 - (b^2 - a^2) \sin^2 \phi]}{[(c^2 - b^2) + (b^2 - a^2) \sin^2 \phi][-\beta + (b^2 - a^2) \sin^2 \phi]} \right\}^{1/2} |d\phi| \\
 &= \int_{\psi_1}^{\psi} \left\{ \frac{b^2 + (c^2 - b^2) \sin^2 \psi}{[(b^2 - a^2) + (c^2 - b^2) \sin^2 \psi][\beta + (c^2 - b^2) \sin^2 \psi]} \right\}^{1/2} |d\psi|
 \end{aligned}
 \tag{96}$$

where $b^2 - a^2 > \beta > b^2 - c^2$. Note that the absolute values of $d\phi$ and $d\psi$ are used in Equation (96).

To define the ranges of ϕ and ψ , it is necessary to go back to Equations (79a), (79b) and (79c). With $\xi=0$ and in terms of ϕ and ψ , they can be rewritten as

$$x = \frac{a}{(c^2 - a^2)^{1/2}} \cos \phi (b^2 \cos^2 \psi + c^2 \sin^2 \psi - a^2)^{1/2} \tag{97a}$$

$$y = b \sin \phi \sin \psi \tag{97b}$$

$$z = \frac{c}{(c^2 - a^2)^{1/2}} \cos \psi (c^2 - a^2 \sin^2 \phi - b^2 \cos^2 \phi)^{1/2} . \tag{97c}$$

If the geodesic path, Equation (96), crosses the curve $\phi=0$ or π , then $\beta < 0$ and if it crosses the curve $\psi=0$ or π , then $\beta > 0$. Thus to ensure the continuity of ϕ and ψ along the geodesic path, the ranges of ϕ and ψ will be defined as follows:

$0 \leq \psi \leq \pi, -\pi \leq \phi \leq 2\pi$ for $\beta < 0$
 and $-\pi \leq \psi \leq 2\pi, 0 \leq \phi \leq \pi$ for $\beta > 0$.

Figure 14 illustrates the ϕ and ψ curves as projected onto the x-z plane. Equation (96) is the geodesic path solution of an ellipsoid which is employed for obtaining more elaborate geodesic paths. When the geodesic path includes one of those four points, P_1, P_2, P_3 and P_4 in Figure 14, then β must equal zero and the integrals in Equation (96) diverge at those points. Thus if $(\phi_2, \psi_2) = P_i, i = 1, 2, 3, 4$, then it is necessary to replace (ϕ_2, ψ_2) by $(\phi_2 + \Delta\phi, \psi_2 + \Delta\psi)$ where $\Delta\phi \neq 0$ and $\Delta\psi \neq 0$. The geodesic path between the two points (ϕ_1, ψ_1) and (ϕ_2, ψ_2) can be determined from Equation (96) by first determining the value of β . Since there are absolute-value signs attached to the differential $d\phi$ and $d\psi$ in the geodesic path solution, it is important to know how the variables ϕ and ψ change from ϕ_1 to ϕ_2 and ψ_1 to ψ_2 , respectively.

CHAPTER V

RESULTS

Geodesics for a source mounted on an ellipsoid can be analyzed precisely by computing the geodesic path defined by the surface parameters (θ_0, ϕ_0) and the geodesic tangent defined by the radial vector direction $(\hat{\theta}_t, \hat{\phi}_t)$ as shown in Figures 15(a) and (b). The geodesic path indicates the actual diffraction point location on an ellipsoid; whereas, the geodesic tangent indicates the radiation direction at the corresponding diffraction point.

To show the validity of the elliptic cylinder perturbation solution, the source is placed at $\theta_s = 90^\circ$ and the geodesic paths and

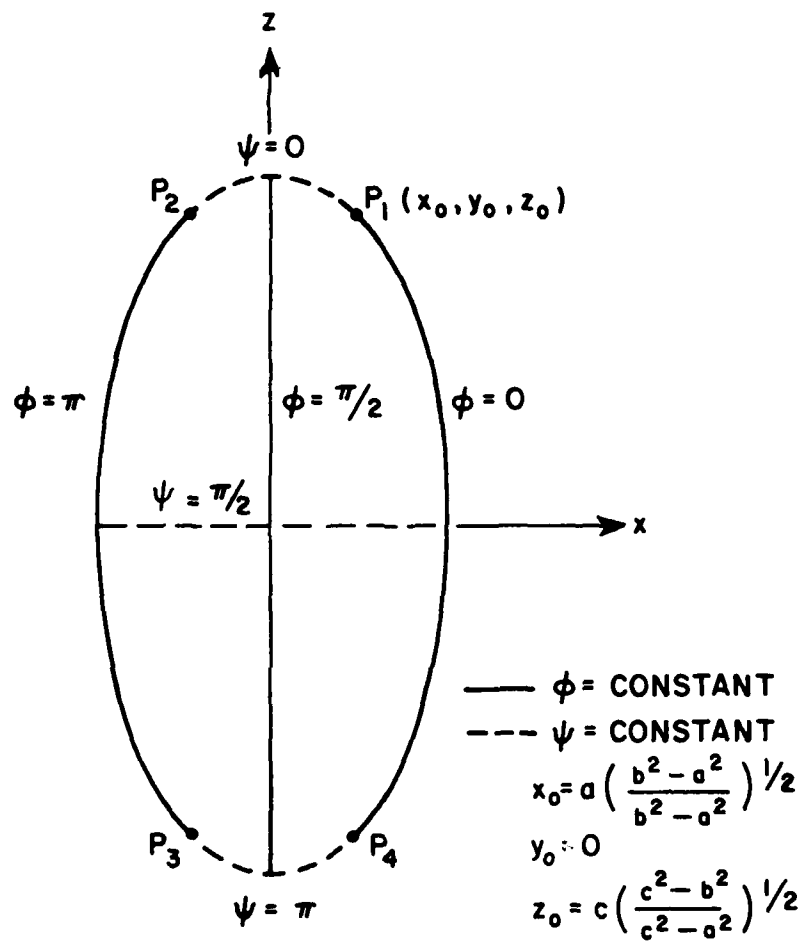


Figure 14. Projection of ϕ - and ψ - curves onto the xz plane of an ellipsoid.

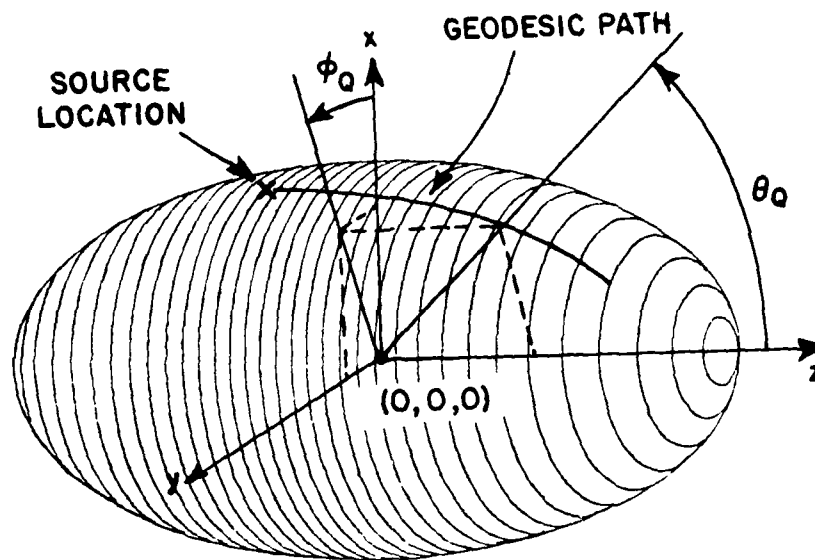


Figure 15(a). Illustration of the geodesic path defined by the surface parameters (θ_Q, ϕ_Q) for a source mounted on an ellipsoid.

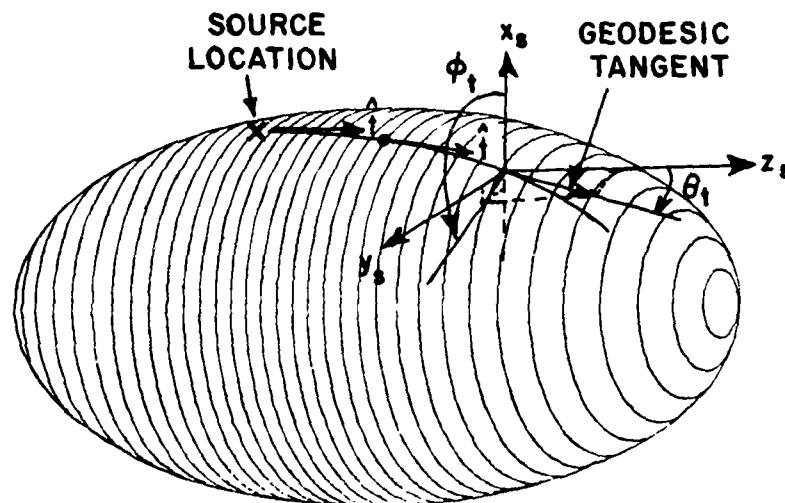


Figure 15(b). Illustration of the geodesic tangent defined by the radial vector direction (θ_t, ϕ_t) for a source mounted on an ellipsoid.

geodesic tangents associated with this source location are calculated as shown in Figures 16(a) through (d) and 17(a) through (d), respectively. In each figure, the elliptic cylinder perturbation solutions are compared with the exact solutions. Looking through those figures, one can see that the geodesic paths and the geodesic tangents of both methods coincide with each other within the significant energy region close to the source. This coincidence in the significant region can be checked more precisely by calculating the Fock parameter (ξ) along each geodesic path as shown in Figures 16(d) and 17(d). Actually, the Fock functions associated with the solutions drop more than 20db as the Fock parameter (ξ) reaches 2.5 in the deep shadow region. This clearly shows the significant portion of the surface as discussed in Chapter I. It is also noted that the geodesic paths on the $2\lambda \times 3\lambda \times 20\lambda$ ellipsoid shown in Figures 16(b) and 17(b) show better agreement than those on the $2\lambda \times 3\lambda \times 4\lambda$ ellipsoid shown in Figures 16(a) and 17(a). Thus, the solution becomes more correct for shapes which are more cylindrical. So one would expect that this approximate solution will work quite successfully for more realistic aircraft and missile shapes which tend to be more cylindrical.

The elliptic cone perturbation solutions can be examined by placing the source at $\theta_s = 30^\circ$ as shown in Figures 18(a) through (c), where the geodesic paths of the elliptic cone perturbation solutions are compared with those of the exact solutions for three different ellipsoid geometries. One should note the good agreement between the two results. The significant energy region of the geodesic paths is shown using the calculated Fock parameters (ξ) in Figure 18(c). It is also noted that

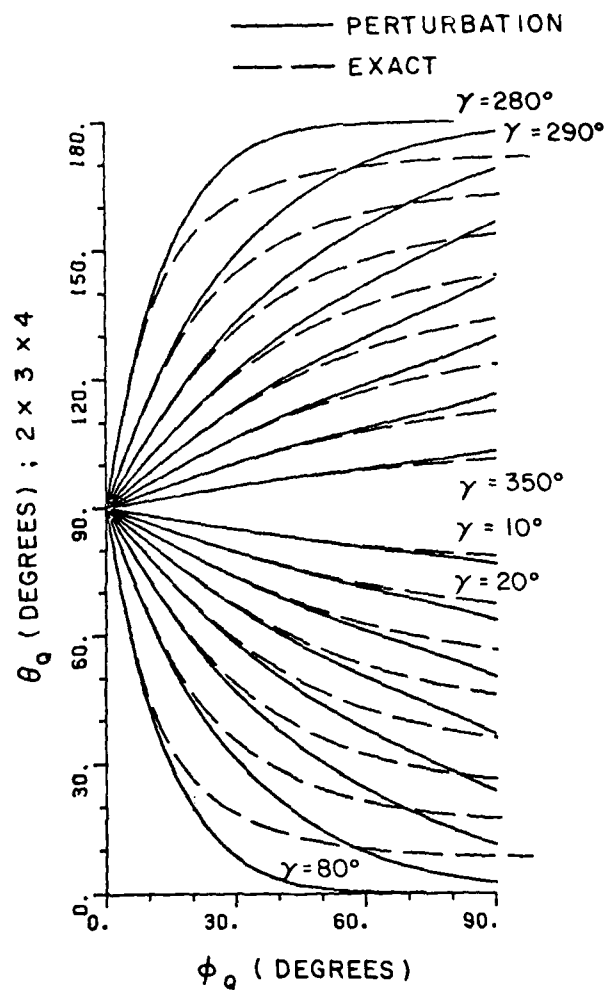


Figure 16(a). Geodesic paths defined by the surface parameters (θ_Q, ϕ_Q) for a source mounted at $\theta_S=90^\circ$ on a $2\lambda \times 3\lambda \times 4\lambda$ ellipsoid. Note that γ is the angle between the geodesic tangent \hat{t} and one principal direction \hat{t}_r at the source location.

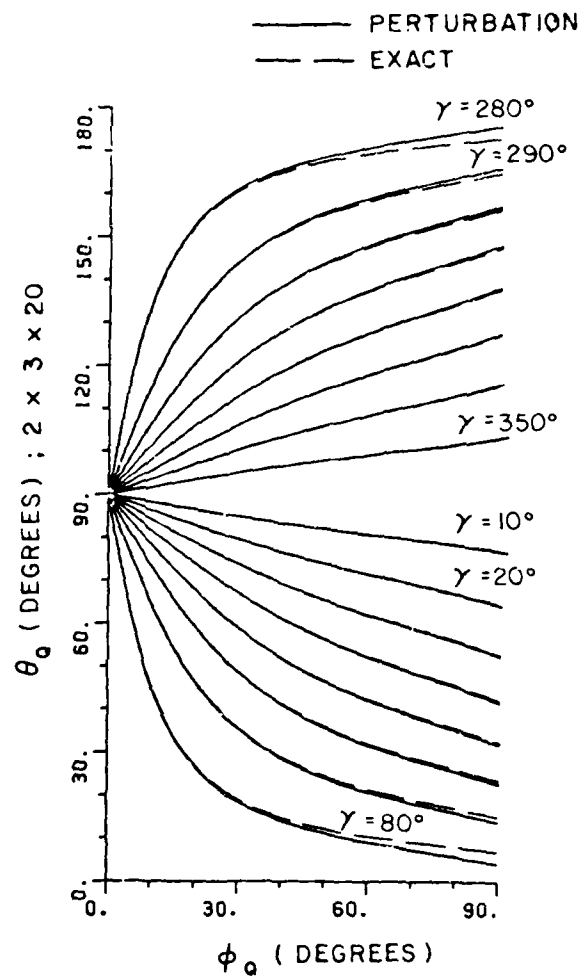


Figure 16(b). Geodesic paths defined by the surface parameters (θ_0, ϕ_0) for a source mounted at $\theta_s = 90^\circ$ on a $2\lambda \times 3\lambda \times 20\lambda$ ellipsoid.

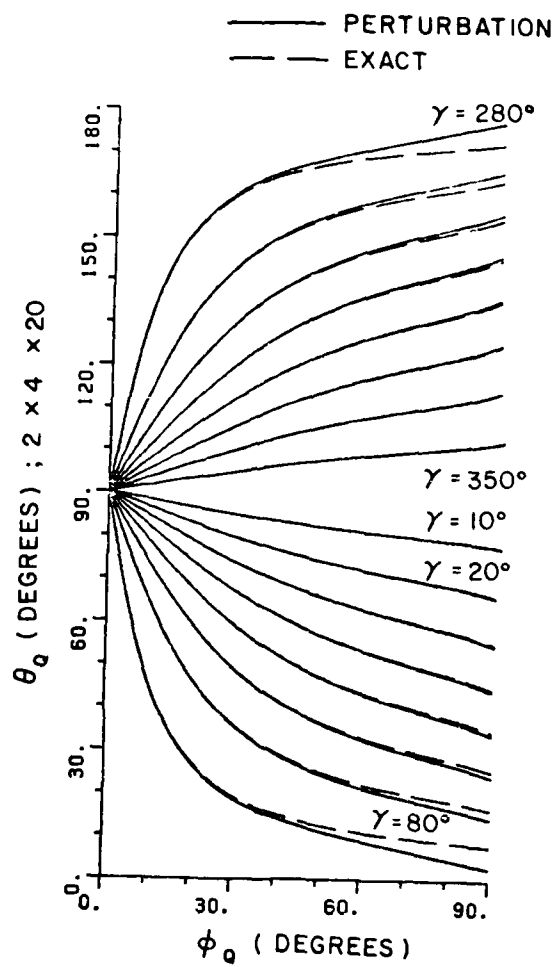


Figure 16(c). Geodesic paths defined by the surface parameters (θ_Q, ϕ_Q) for a source mounted at $\theta_S=90^\circ$ on a $2\lambda \times 4\lambda \times 20\lambda$ ellipsoid.

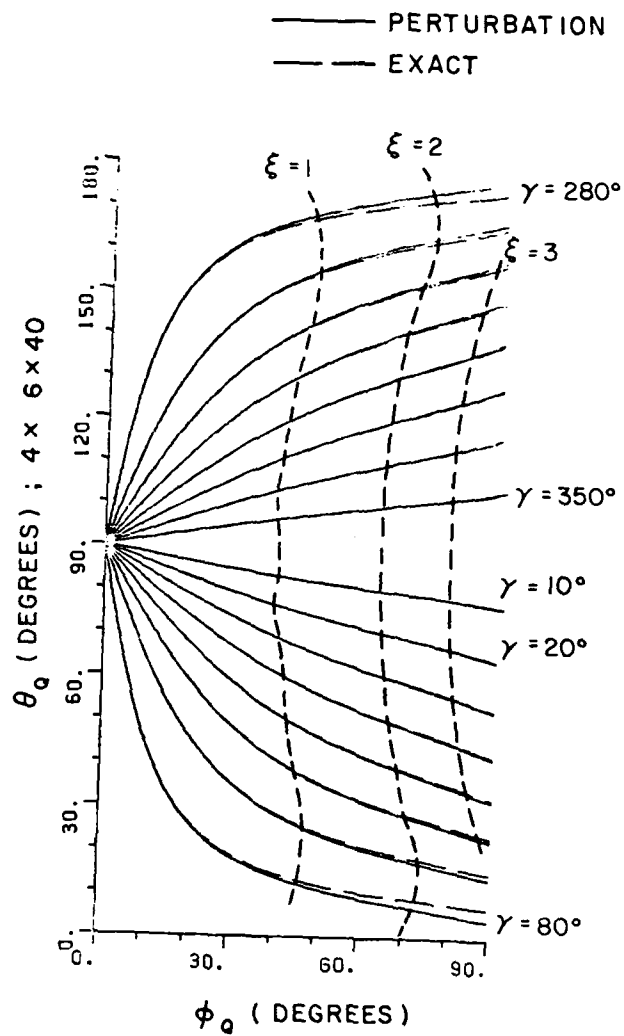


Figure 16(d). Geodesic paths defined by the surface parameters (θ_Q, ϕ_Q) for a source mounted at $\theta_S=90^\circ$ on a $4\lambda \times 6\lambda \times 40\lambda$ ellipsoid.

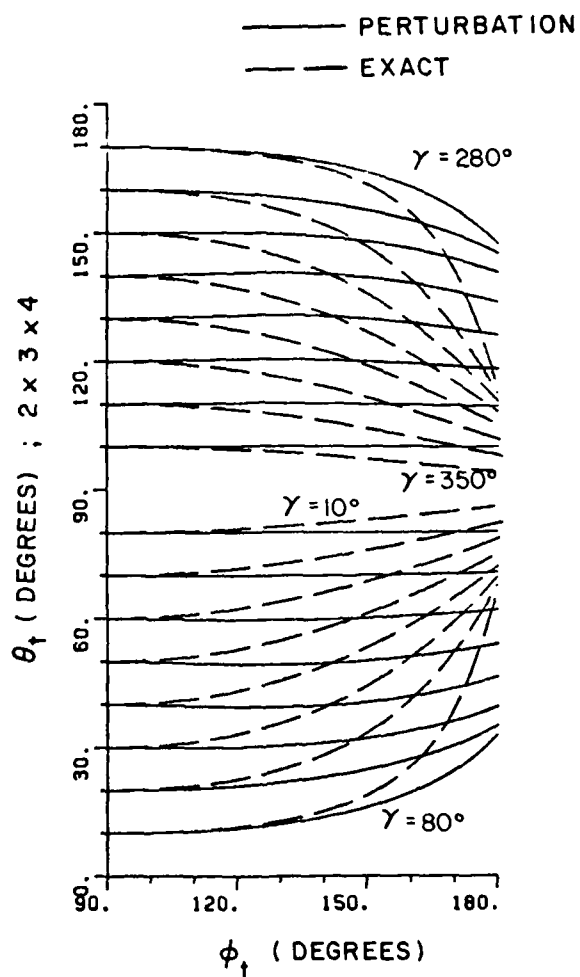


Figure 17(a). Geodesic tangents defined by the radial vector direction (θ_t, ϕ_t) for a source mounted at $\theta_s = 90^\circ$ on a $2\lambda \times 3\lambda \times 4\lambda$ ellipsoid. Note that γ is the angle between the geodesic tangent \hat{t} and one principal direction \hat{t}_r at the source location.

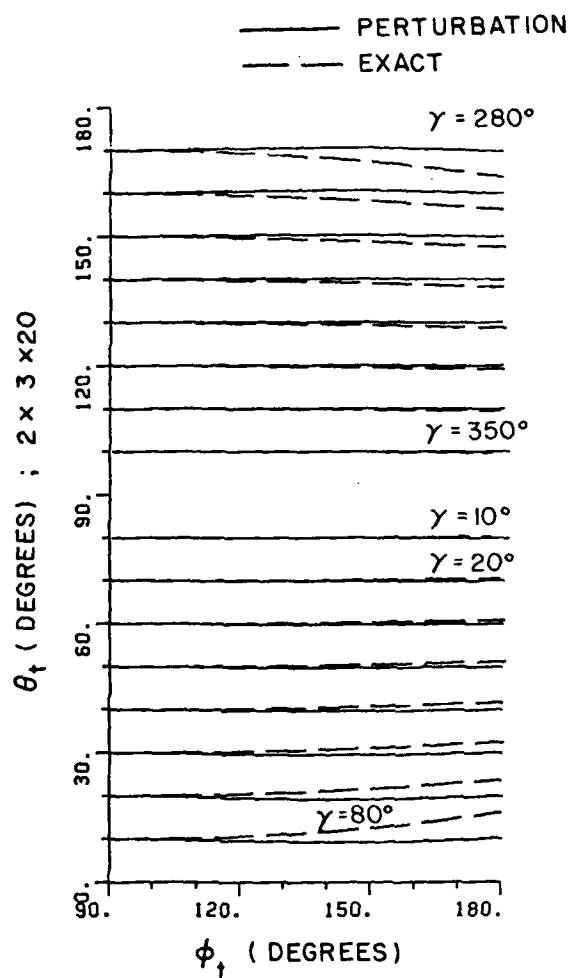


Figure 17(b). Geodesic tangents defined by the radial vector direction (θ_t, ϕ_t) for a source mounted at $\theta_s = 90^\circ$ on a $2\lambda \times 3\lambda \times 20\lambda$ ellipsoid.

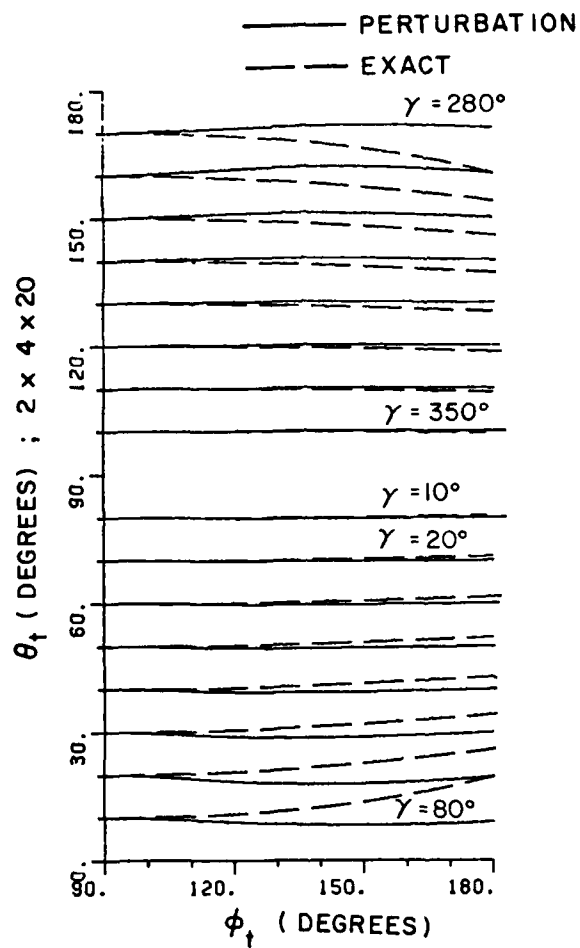


Figure 17(c). Geodesic tangents defined by the radial vector direction (θ_t, ϕ_t) for a source mounted at $\theta_s = 90^\circ$ on a $2\lambda \times 4\lambda \times 20\lambda$ ellipsoid.

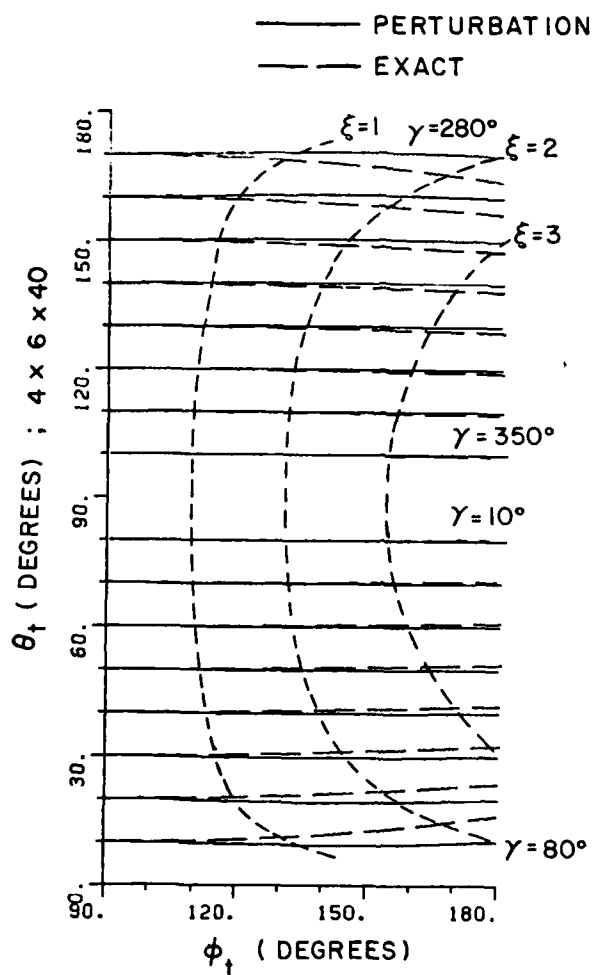


Figure 17(d). Geodesic tangents defined by the radial vector direction (θ_t, ϕ_t) for a source mounted at $\theta_s = 90^\circ$ on a $4\lambda \times 6\lambda \times 40\lambda$ ellipsoid.

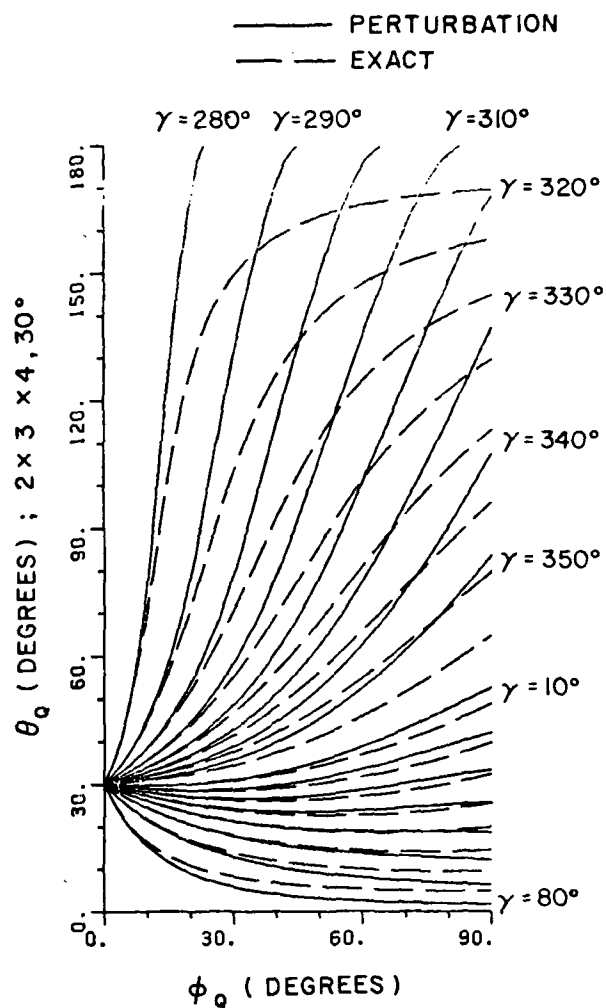


Figure 18(a). Geodesic paths defined by the surface parameters (θ_Q, ϕ_Q) for a source mounted at $\theta_S = 30^\circ$ on a $2\lambda \times 3\lambda \times 4\lambda$ ellipsoid. Note that γ is the angle between the geodesic tangent \hat{t} and one principal direction \hat{t}_r at the source location.

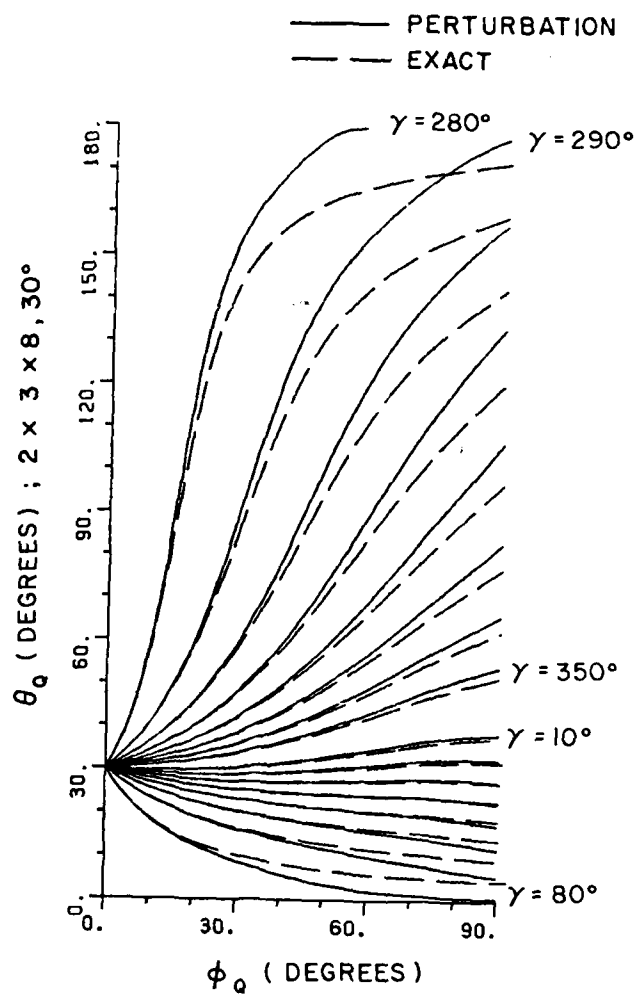


Figure 18(b). Geodesic paths defined by the surface parameters (θ_Q, ϕ_Q) for a source mounted at $\theta_S=30^\circ$ on a $2\lambda \times 3\lambda \times 8\lambda$ ellipsoid.

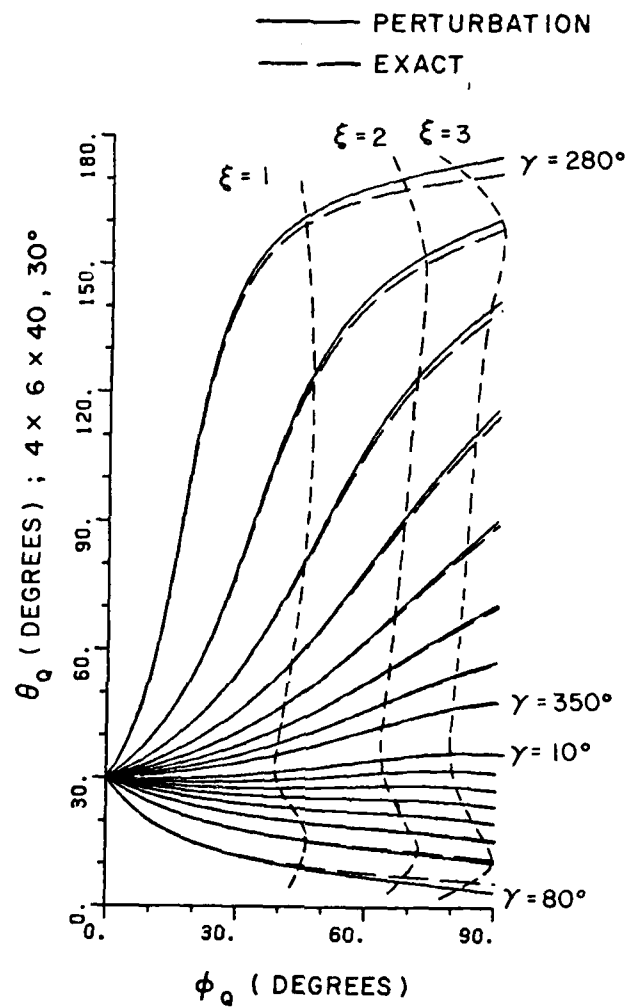


Figure 18(c). Geodesic paths defined by the surface parameters (θ_Q, ϕ_Q) for a source mounted at $\theta_S = 30^\circ$ on a $4\lambda \times 6\lambda \times 40\lambda$ ellipsoid.

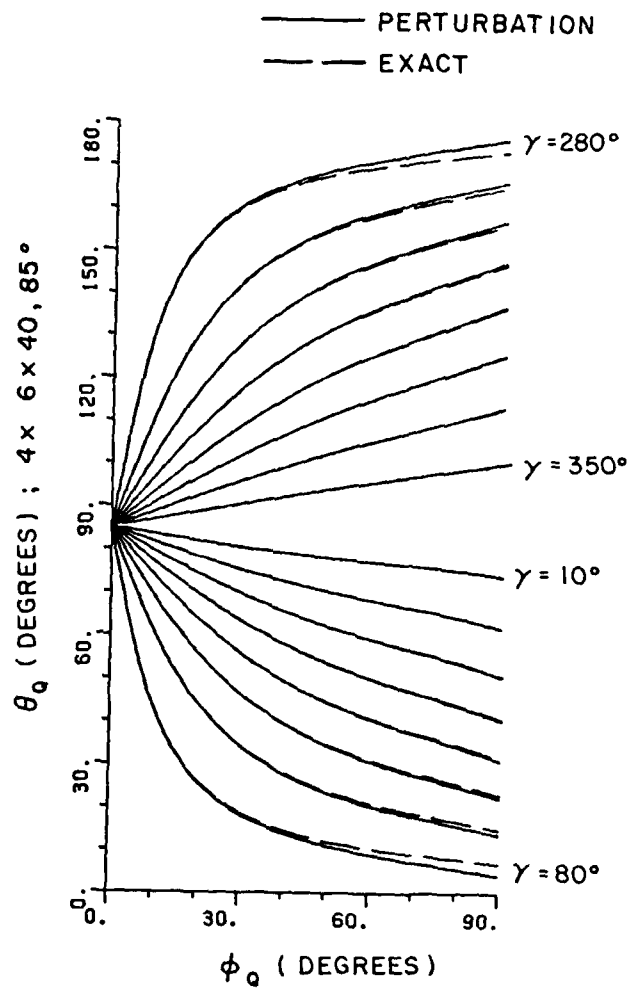


Figure 18(d). Geodesic paths defined by the surface parameters (θ_0, ϕ_0) for a source mounted at $\theta_s = 85^\circ$ on a $4\lambda \times 6\lambda \times 40\lambda$ ellipsoid.

the geometry of the ellipsoid used in Figure 18(c) is more realistic in terms of simulating an aircraft or missile fuselage than those used in Figure 18(a) and (b). To make sure that the solution switches correctly between the elliptic cylinder and the elliptic cone perturbation method, the source is placed at $\theta_s = 85^\circ$ and the geodesic paths are calculated as shown in Figure 18(d). Comparing Figure 18(d) with Figure 16(d), one can see that the geodesic paths of the elliptic cone perturbation solution are very close to those of the elliptic cylinder perturbation solution for that source location.

In Figures 19(a) through (p), the geodesic tangents obtained by the elliptic cone perturbation solution are compared with those of the exact solutions for several different source locations and ellipsoid geometries. As one moves the source location away from the two ends of the ellipsoid, one can see that the discrepancies between perturbation solutions and exact solutions become smaller as shown in the sequence of figures, i.e., Figures 19(a), (b), (c) and (d). In order to provide more information about the applicable geometries and source locations, several different geometries and source locations are examined in Figures 19(e) through (o). For the more realistic case, i.e., the $4\lambda \times 6\lambda \times 40\lambda$ ellipsoid, with the source location $\theta_s = 30^\circ$ is plotted in Figure 19(p). Although one can see small discrepancies for the rays toward the tips of the ellipsoid, i.e., lines for $\gamma = 80^\circ$ and $\gamma = 280^\circ$ in the Figure 19(p), they only happen when the caustic effects come into play. In the caustic region where virtually an infinite set of rays have significant effects on the radiation pattern, the basic GTD theory fails. The study of this caustic effect is beyond the scope of this

study. If one neglects the caustic regions, the geodesic tangents using the perturbation model shown in Figure 19(p) coincide with the exact solution very well in the significant region.

CHAPTER VI

SUMMARY AND CONCLUSIONS

The object of this study is to develop an efficient numerical technique to calculate the geodesic paths of an ellipsoid-mounted antenna. The Geometrical Theory of Diffraction is the basic approach applied here. The curved surface diffraction solutions are discussed in Chapter II, where the creeping wave solutions in the shadow region are of particular interest.

Elliptic cylinder and elliptic cone perturbation methods are presented in Chapter III to simulate the geodesic paths on an ellipsoid, which in turn can be used to model an aircraft or missile fuselage. Because the elliptic cylinder and elliptic cone are developed surfaces, the geodesic paths can be found on an unfolded planar surface.

In order to show the validity of the perturbation solutions, more elaborate numerical method for the geodesic paths employing calculus of variations, whose results are indicated as exact solutions here, is also presented in Chapter IV. Although this method provides accurate geodesic paths on the ellipsoid, it is too complicated and inefficient to use for practical radiation applications. However, the exact solution is most appropriate for coupling problems where the exact path is desired between two known points on the surface.

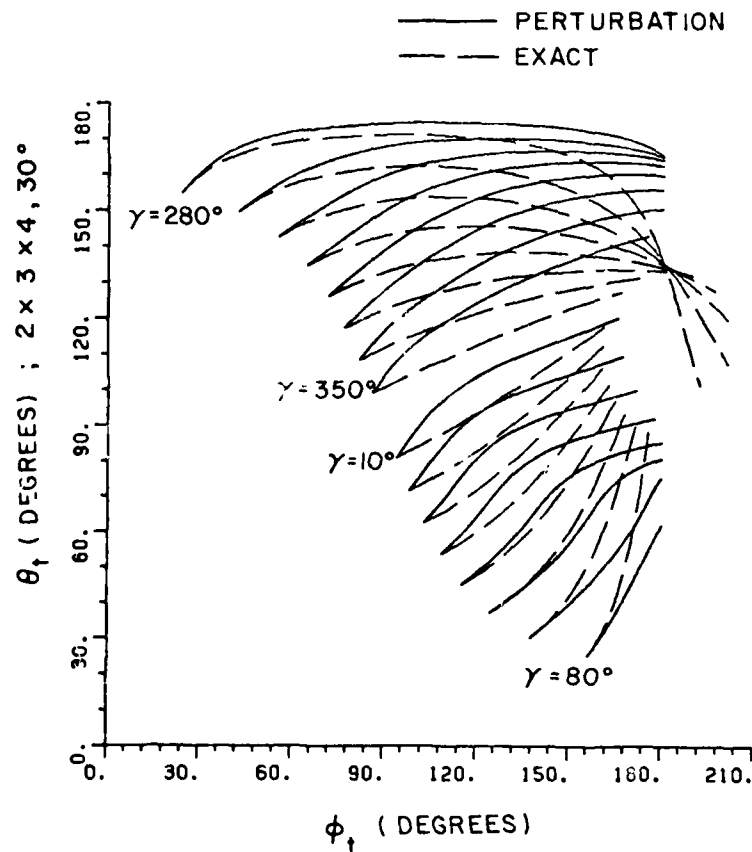


Figure 19(a). Geodesic tangents defined by the radial vector direction (θ_t, ϕ_t) for a source mounted at $\theta_s = 30^\circ$ on a $2\lambda \times 3\lambda \times 4\lambda$ ellipsoid. Note that γ is the angle between the geodesic tangent \hat{t} and one principal direction \hat{t}_r , at the source location.

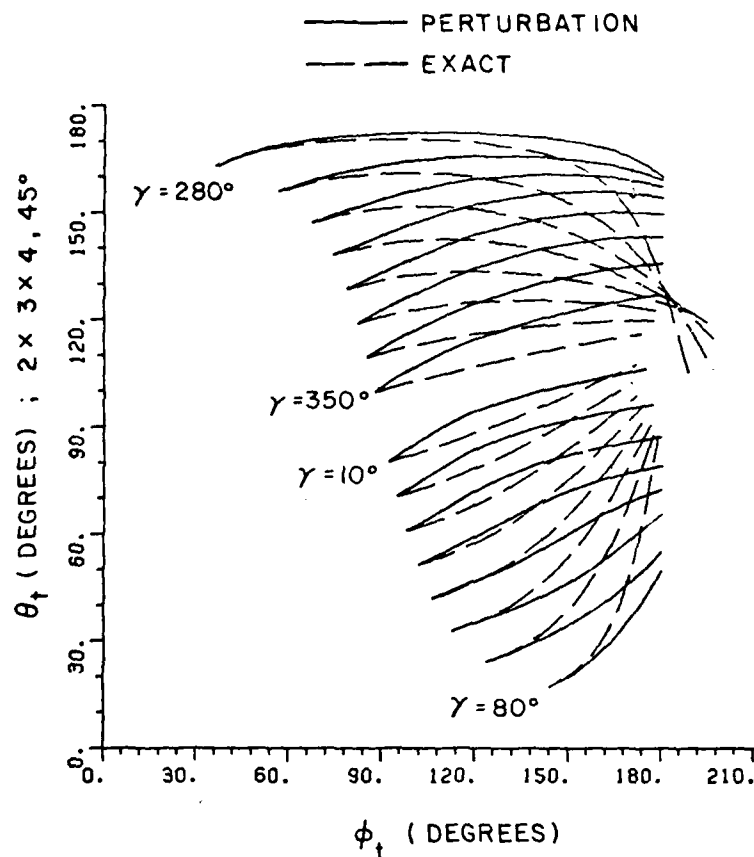


Figure 19(b). Geodesic tangents defined by the radial vector direction (θ_t, ϕ_t) for a source mounted at $\theta_s = 45^\circ$ on a $2\lambda \times 3\lambda \times 4\lambda$ ellipsoid.

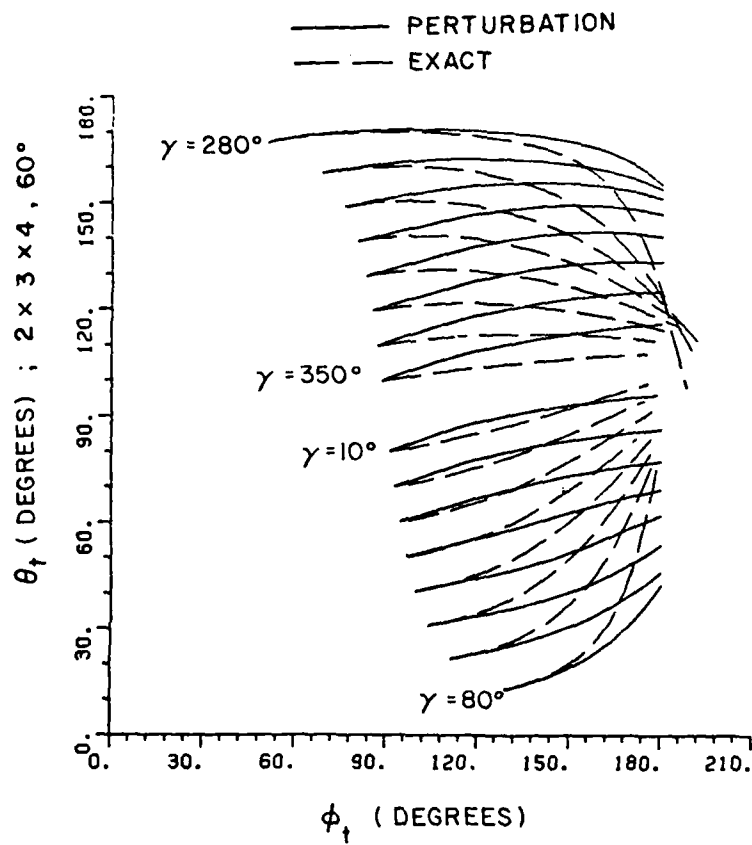


Figure 19(c). Geodesic tangents defined by the radial vector direction (θ_t, ϕ_t) for a source mounted at $\theta_s = 60^\circ$ on a $2\lambda \times 3\lambda \times 4\lambda$ ellipsoid.

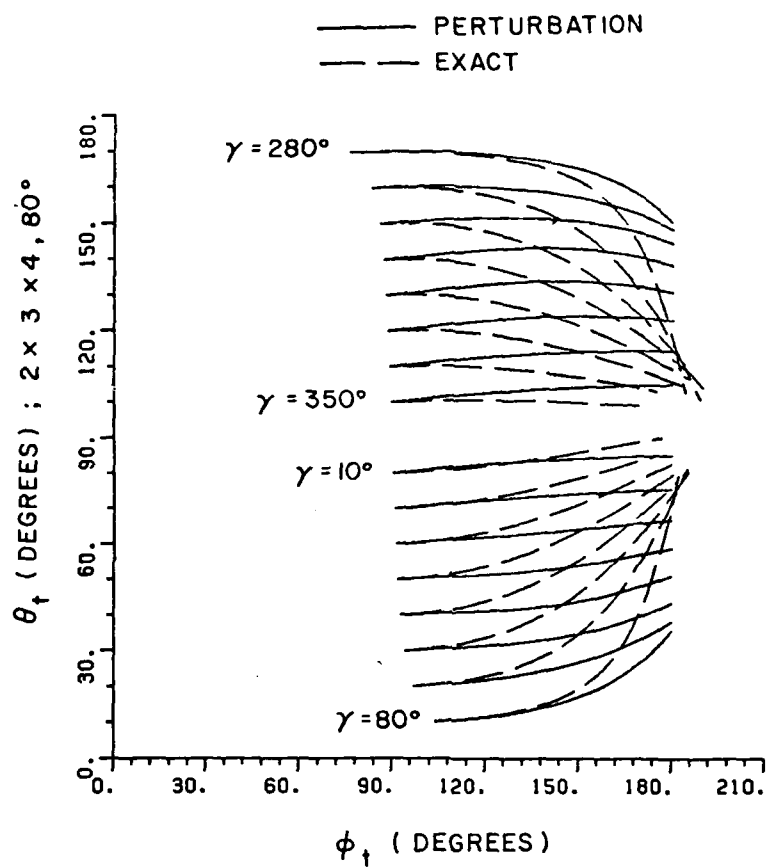


Figure 19(d). Geodesic tangents defined by the radial vector direction (θ_t, ϕ_t) for a source mounted at $\theta_s=80^\circ$ on a $2\lambda \times 3\lambda \times 4\lambda$ ellipsoid.

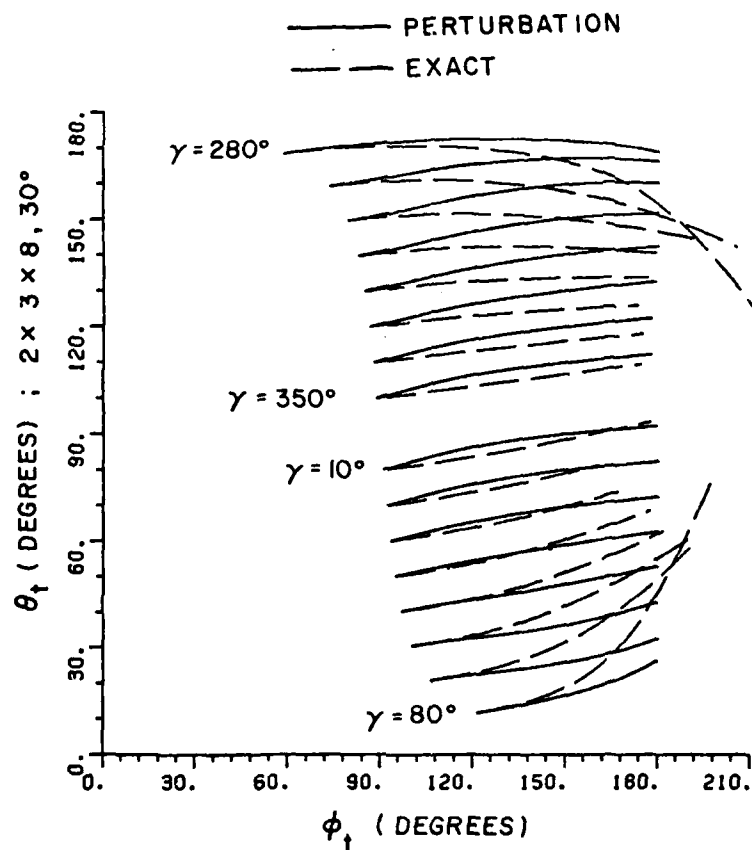


Figure 19(e). Geodesic tangents defined by the radial vector direction (θ_t, ϕ_t) for a source mounted at $\theta_s = 30^\circ$ on a $2\lambda \times 3\lambda \times 8\lambda$ ellipsoid.

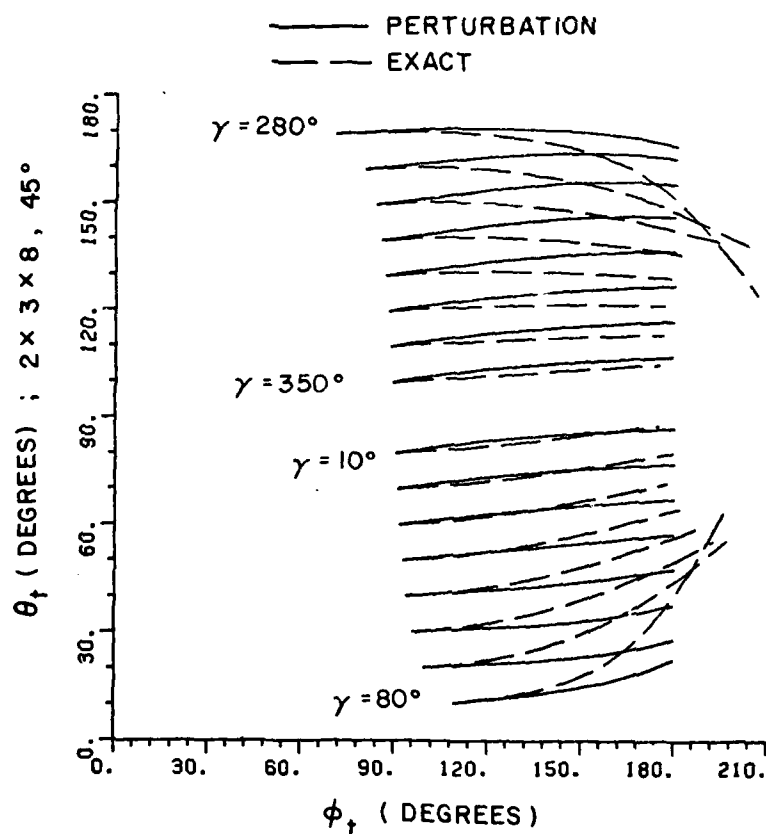


Figure 19(f). Geodesic tangents defined by the radial vector direction (θ_t, ϕ_t) for a source mounted at $\theta_s = 45^\circ$ on a $2\lambda \times 3\lambda \times 8\lambda$ ellipsoid.

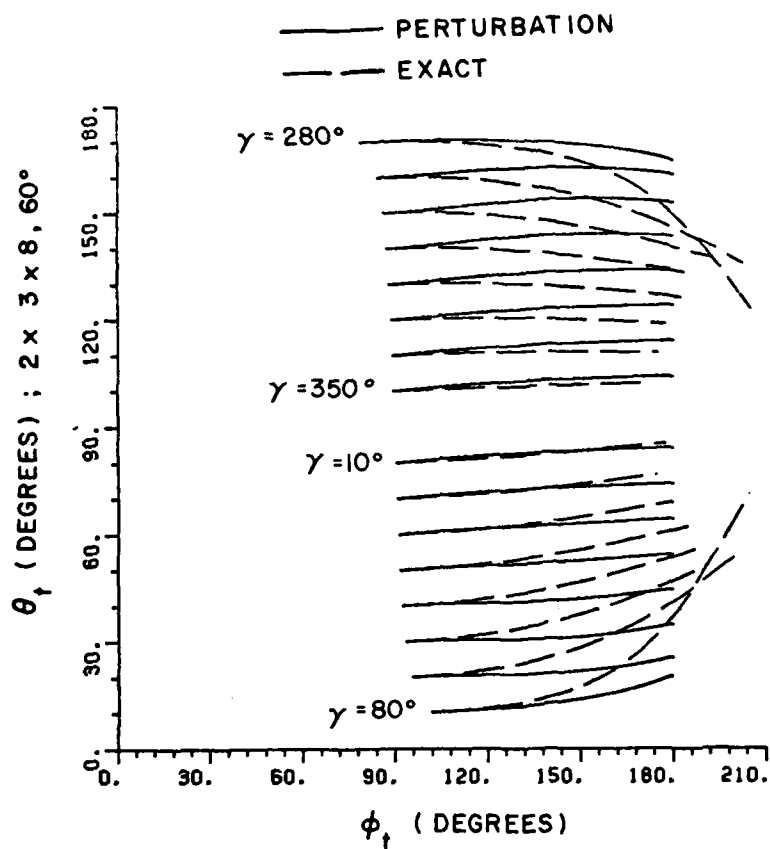


Figure 19(g). Geodesic tangents defined by the radial vector direction (θ_t, ϕ_t) for a source mounted at $\theta_s=60^\circ$ on a $2\lambda \times 3\lambda \times 8\lambda$ ellipsoid.

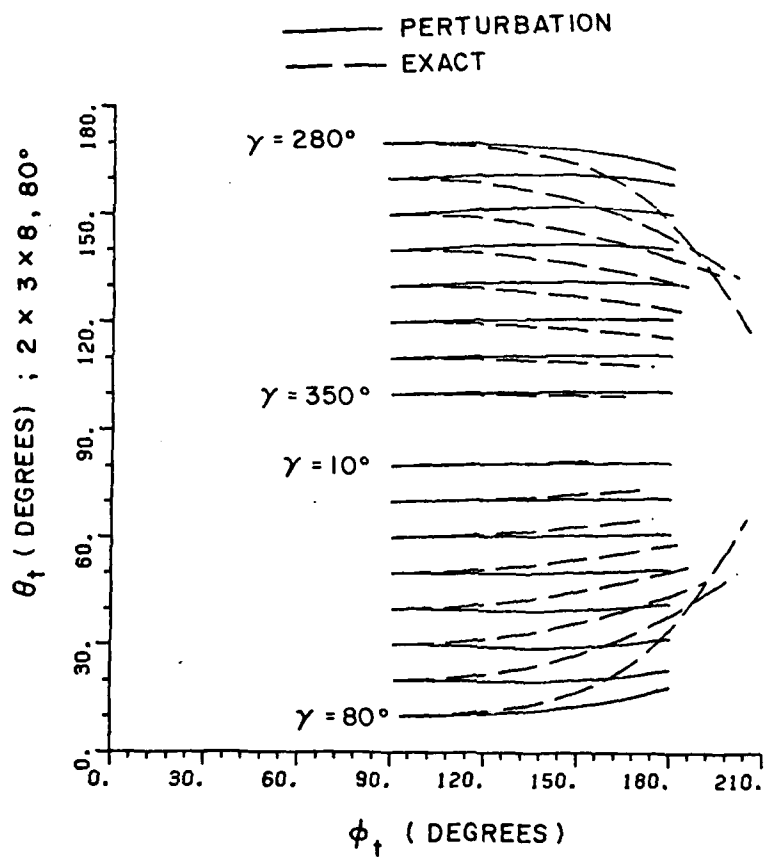


Figure 19(h). Geodesic tangents defined by the radial vector direction (θ_t, ϕ_t) for a source mounted at $\theta_s=80^\circ$ on a $2\lambda \times 3\lambda \times 8\lambda$ ellipsoid.

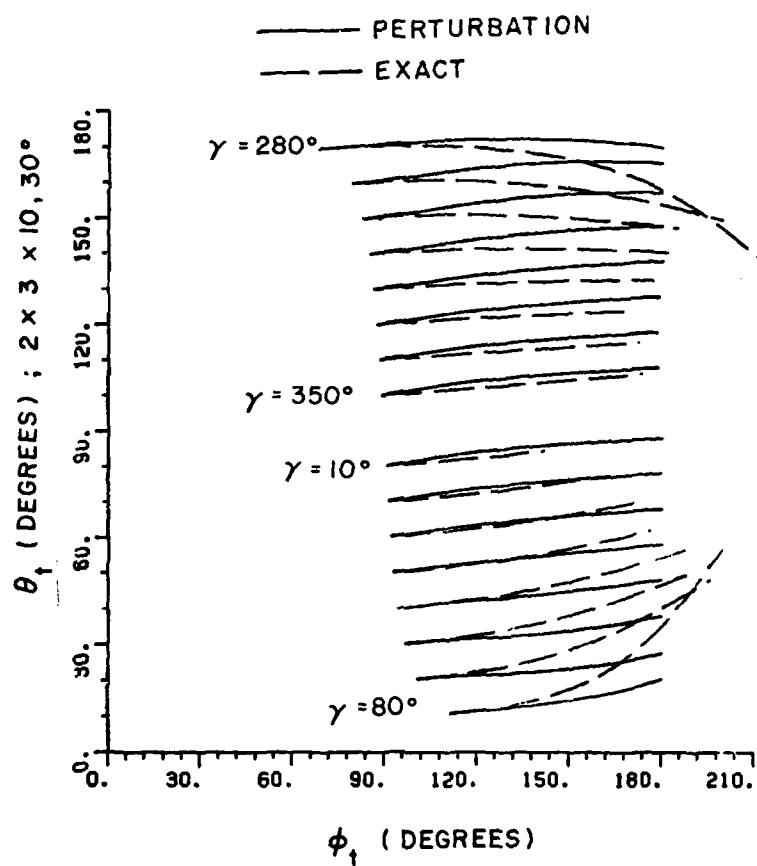


Figure 19(i). Geodesic tangents defined by the radial vector direction (θ_t , ϕ_t) for a source mounted at $\theta_s = 30^\circ$ on a $2\lambda \times 3\lambda \times 10\lambda$ ellipsoid.

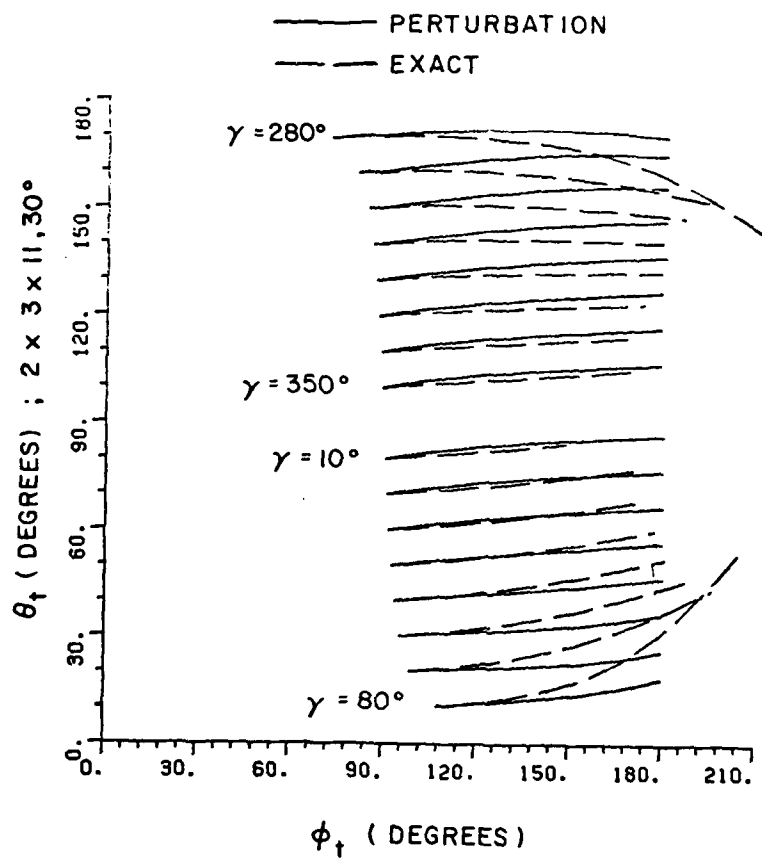


Figure 19(j). Geodesic tangents defined by the radial vector direction (θ_t, ϕ_t) for a source mounted at $\theta_s=30^\circ$ on a $2\lambda \times 3\lambda \times 11\lambda$ ellipsoid.

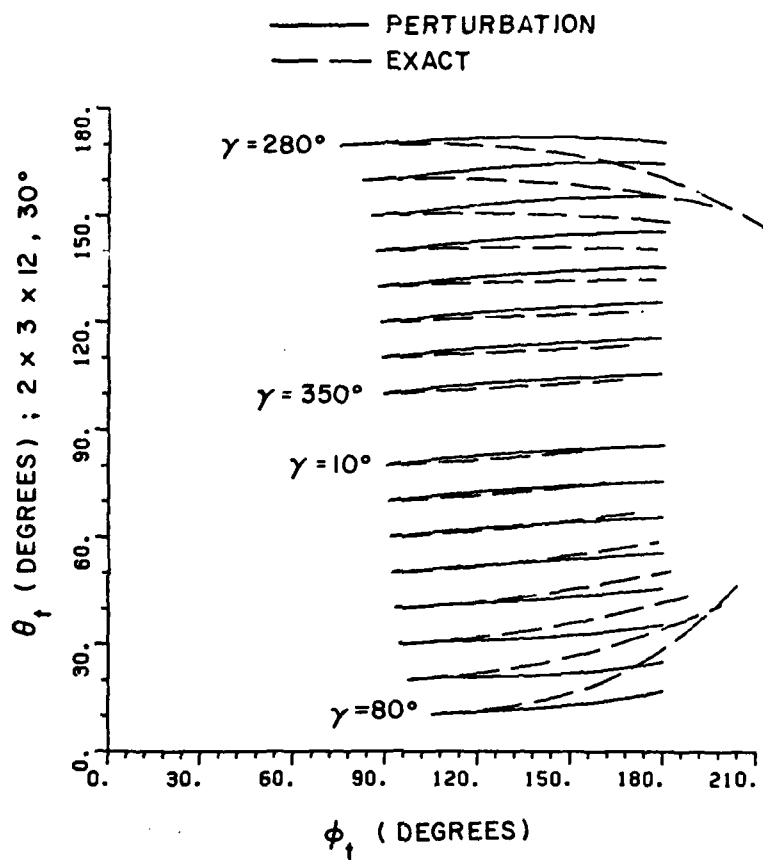


Figure 19(k). Geodesic tangents defined by the radial vector direction (θ_t, ϕ_t) for a source mounted at $\theta_s = 30^\circ$ on a $2\lambda \times 3\lambda \times 12\lambda$ ellipsoid.

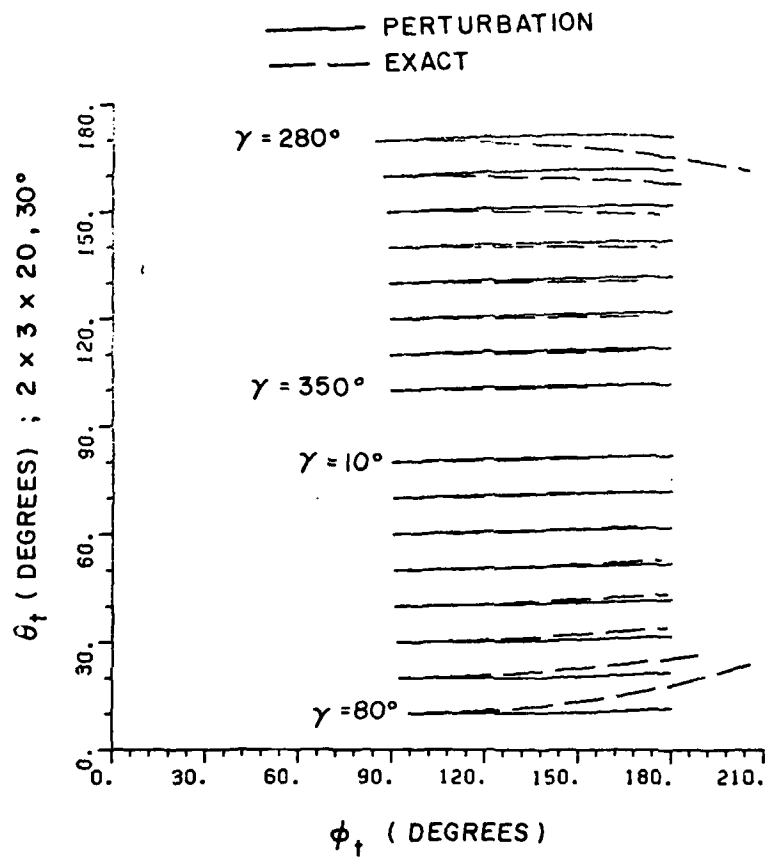


Figure 19(1). Geodesic tangents defined by the radial vector direction (θ_t, ϕ_t) for a source mounted at $\theta_s = 30^\circ$ on a $2\lambda \times 3\lambda \times 20\lambda$ ellipsoid.

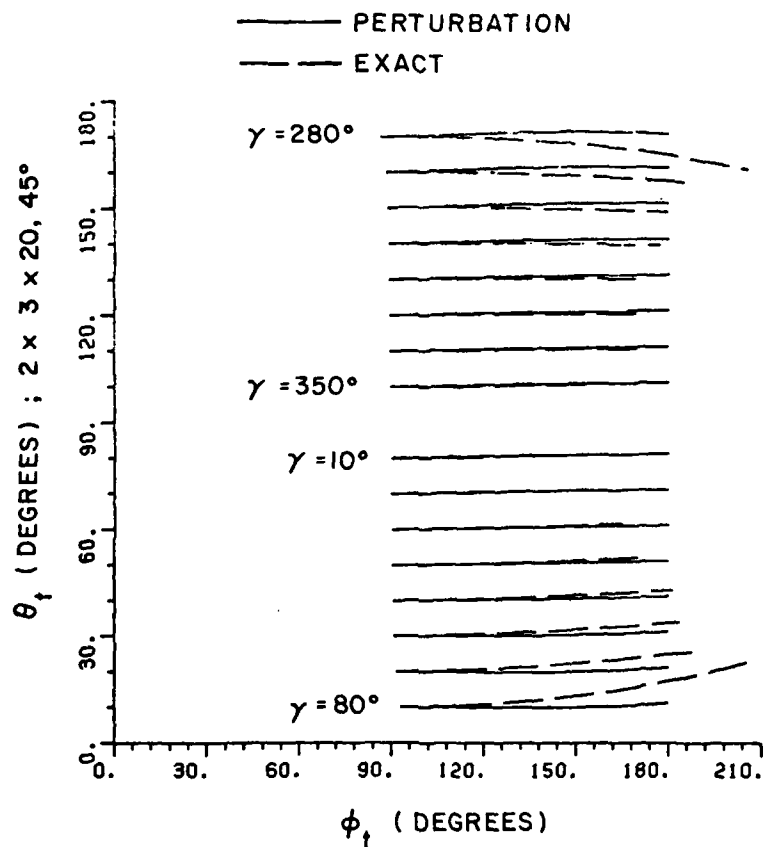


Figure 19(m). Geodesic tangents defined by the radial vector direction (θ_t, ϕ_t) for a source mounted at $\theta_s = 45^\circ$ on a $2\lambda \times 3\lambda \times 20\lambda$ ellipsoid.

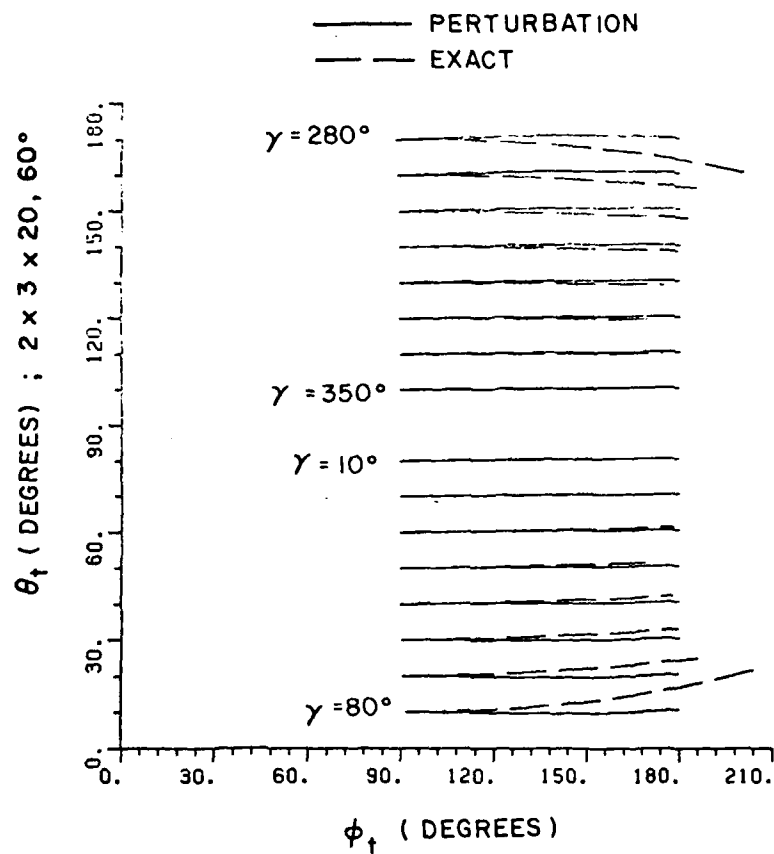


Figure 19(n). Geodesic tangents defined by the radial vector direction (θ_t, ϕ_t) for a source mounted at $\theta_s = 60^\circ$ on a $2\lambda \times 3\lambda \times 20\lambda$ ellipsoid.

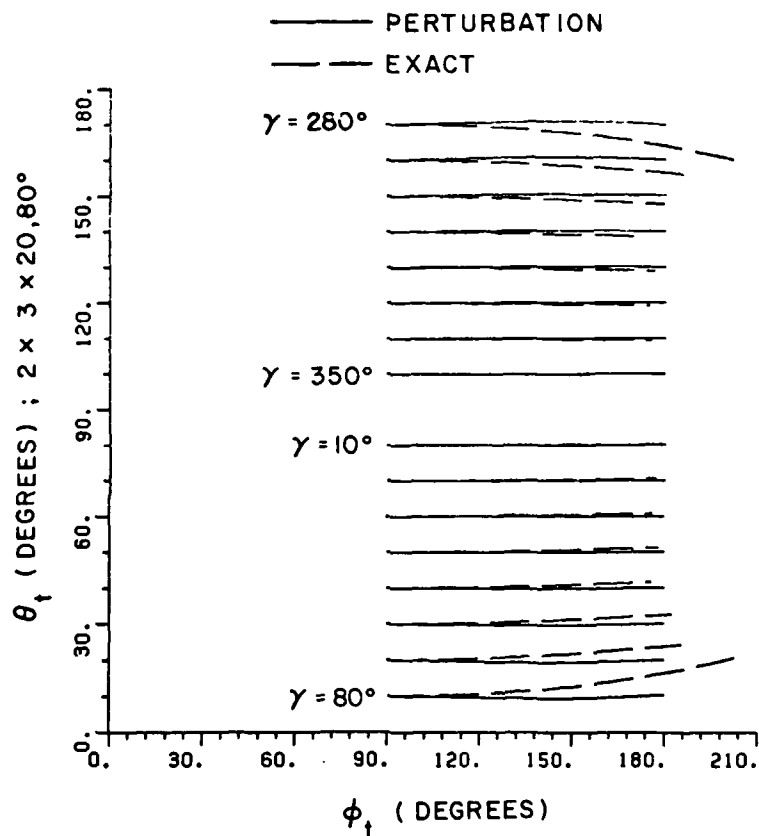


Figure 19(o). Geodesic tangents defined by the radial vector direction (θ_t, ϕ_t) for a source mounted at $\theta_s = 80^\circ$ on a $2\lambda \times 3\lambda \times 20\lambda$ ellipsoid.

AD-A116 453

OHIO STATE UNIV COLUMBUS ELECTROSCIENCE LAB
GEODESIC PATHS OF AN ELLIPSOID-MOUNTED ANTENNA. (U)
MAR 82 J G KIM, N WANG, C D CHUANG
UNCLASSIFIED ESL-714215-1

F/G 9/1

N00019-81-C-0424
NL

2 of 2

DTIC
16-45.5



END
DATE
FILMED
07-82
DTIC

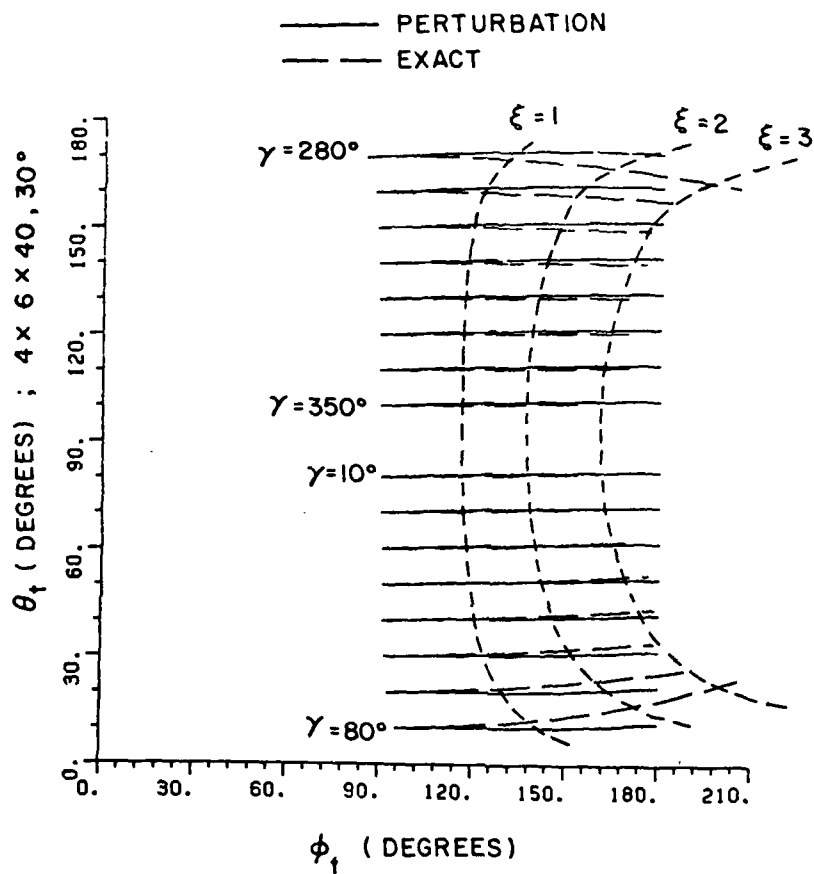


Figure 19(p). Geodesic tangents defined by the radial vector direction (θ_t, ϕ_t) for a source mounted at $\theta_s = 30^\circ$ on a $4\lambda \times 6\lambda \times 40\lambda$ ellipsoid.

The geodesic paths of the perturbation solutions are compared with those of the exact solutions for several different geometries and source locations in Chapter V. The comparison of both results illustrates that the geodesic paths can be solved using either numerical technique; however, the perturbation is much more efficient. In addition, one can easily relate the radiation direction with the desired geodesic path using the perturbation method. On the other hand, one is not sure which geodesic is necessary to achieve the desired radiation direction using the exact solution.

This ellipsoidal model will be applied next to analyze antenna patterns for antennas mounted on aircraft. The ellipsoid will be used to simulate the fuselage.

REFERENCES

1. Burnside, W.D., "Analysis of On-Aircraft Antenna Patterns," August 1972, Report No. 3390-1, The Ohio State University ElectroScience Laboratory, Department of Electrical Engineering, prepared under Contract No. 62269-72-C-0354 for Naval Air Development Center. Also a Dissertation to The Ohio State University.
2. Wang, N. and Burnside, W.D., "An Efficient Geodesic Path Solution for Prolate Spheroids," July 1979, Report No. 711305-2, The Ohio State University ElectroScience Laboratory, Department of Electrical Engineering, prepared under Contract No. N00019-78-C-0524 for Naval Air Systems Command.
3. Pathak, P.H., Wang, N., Burnside, W.D., and Kouyoumjian, R.G., "A Uniform GTD Solution for the Radiation from Sources on a Convex Surface," February 1980, Report No. 711305, The Ohio State University ElectroScience Laboratory, Department of Electrical Engineering, prepared under Contract No. N00019-78-C-0524 for Naval Air Systems Command.
4. Huang, C.C., Wang, N. and Burside, W.D., "The High-Frequency Radiation Patterns of a Spheroid-mounted Antenna," March 1980, Report No. 712527-1, The Ohio State University ElectroScience Laboratory, Department of Electrical Engineering, prepared under Contract No. N00019-80-C-0050 for Naval Air Systems Command.
5. Lipschutz, M.M., Differential Geometry, Schaum's Outline Series, McGraw-Hill Book Co., New York, N.Y., (1969).

6. Burnside, W.D., Wang, N., and Pelton, E.L., "Near Field Pattern Computations for Airborne Antenna," June 1978, Report No. 784685-4, prepared under Contract No. N00019-77-C-0299, Department of the Navy, Naval Air Systems Command.

**DATE
FILMED**

7-8